USGS
science for a changing world

Prepared in cooperation with the U.S. National Park Service

Strontium Isotope Chronostratigraphic Age of a Sirenian Fossil Site on Santa Rosa Island, Channel Islands National Park, California

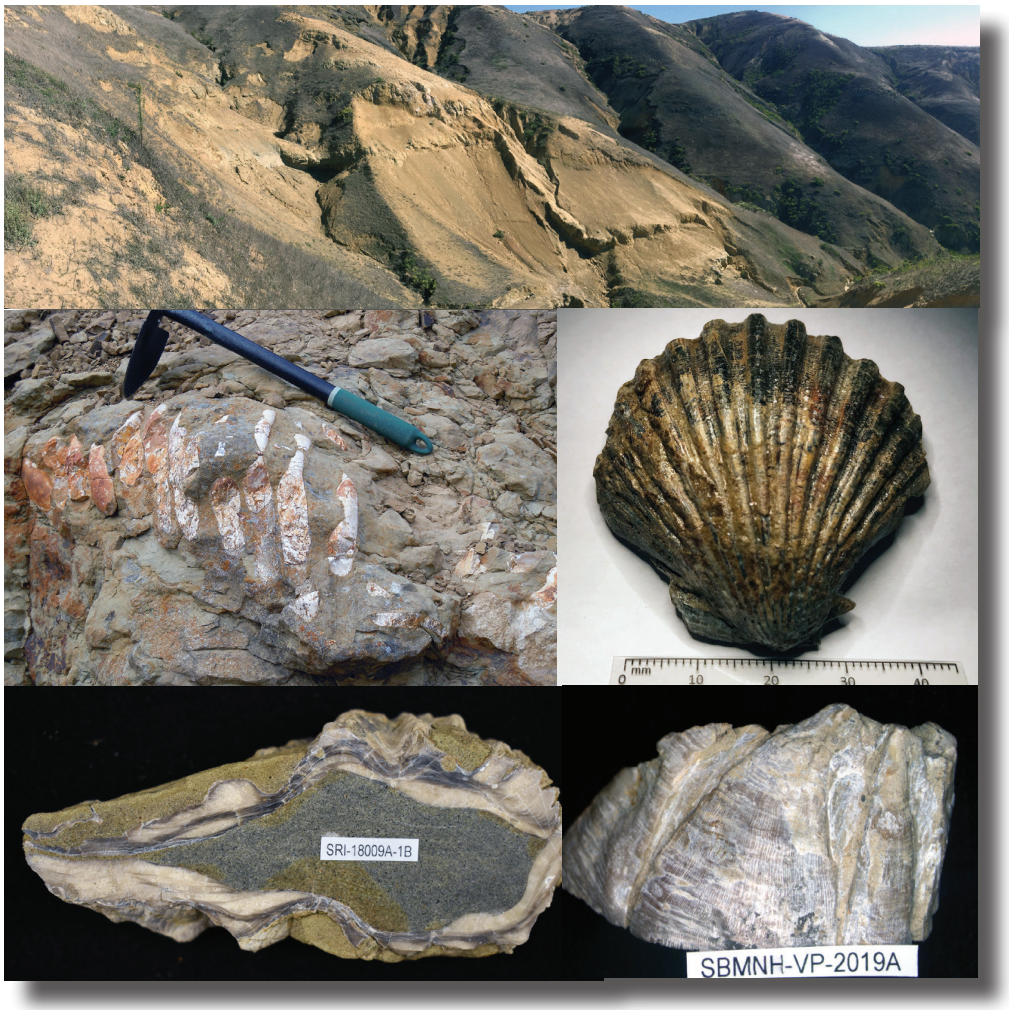

Scientific Investigations Report 2023–5026

U.S. Department of the Interior
U.S. Geological Survey

Cover. Upper photo: Oblique photograph looking east towards the hillside site where sirenian (dugongid) fossils were discovered. Heavily incised terrane is typical of the geomorphological response of Vaqueros Sandstone and Rincon formation sedimentary strata to erosion. Height of the exposed hillslope is about 15 m. Middle left: Photograph showing the partial ribcage of the original dugongid fossil as found in 2012. The pick positioned above the exposed bones has a 0.4-m-long handle. Middle right: Well-preserved fossil *Lyropecten* sp. (scallop) shell used to date sedimentary strata associated with the dugong fossils by seawater-strontium chronostratigraphy. Lower left: Polished cross section of a fully articulated fossil *Pyrodonte* sp. (oyster) shell showing a complex variety of colors and textures. The specimen is encased and infilled with fine sand and silt matrix of the host rock. Shell is about 10 cm long and 4 cm wide at its thickest. Lower right: Fossil *Balanus* sp. (barnacle) specimen showing multiple calcite plates that form a nearly complete carapace. Specimen is about 3 cm in diameter at its base.

Strontium Isotope Chronostratigraphic Age of a Sirenian Fossil Site on Santa Rosa Island, Channel Islands National Park, California

By James B. Paces, Scott A. Minor, Kevin M. Schmidt, and Jonathan Hoffmann

Prepared in cooperation with the U.S. National Park Service

Scientific Investigations Report 2023–5026

U.S. Department of the Interior
U.S. Geological Survey

U.S. Geological Survey, Reston, Virginia: 2023

Suggested citation:
Paces, J.B., Minor, S.A., Schmidt, K.M., and Hoffmann, J., 2023, Strontium isotope chronostratigraphic age of a sirenian fossil site on Santa Rosa Island, Channel Islands National Park, California: U.S. Geological Survey Scientific Investigations Report 2023–5026, 27 p., https://doi.org/10.3133/sir20235026.

Associated data for this publication:
Paces, J.B., 2022, Sr concentrations and $^{87}Sr/^{86}Sr$ data used to determine the Sr-chronostratigraphic age of sirenian fossils on Santa Rosa Island, Channel Islands National Park: California, USA: U.S. Geological Survey data release, https://doi.org/10.5066/P9GG6NB5.

ISSN 2328-0328 (online)

Acknowledgments

This work was supported by the National Cooperative Geologic Mapping Program of the U.S. Geological Survey (USGS) and represents a contribution to the GeoMapping for Integrated Science Project (https://www.usgs.gov/centers/gmeg/science/geomapping-integrated-science). Channel Islands National Park provided in-kind support for fieldwork on Santa Rosa Island and permission to collect samples (task agreement P18AC00955 to Jonathan Hoffman; research-collecting permits for study CHIS-00117 to Scott Minor and Kevin M. Schmidt). Financial support for fieldwork was partly provided by the National Park Service Geologic Resources Division to authors S. Minor and K. Schmidt through Interagency Agreement (16 U.S.C. 460l-1(g)). Gary Skipp (USGS, retired) provided X-ray diffraction analyses of shell subsamples. Thorough technical reviews by Daniel Muhs, Robert Poirier, and Andrew Cyr improved the quality of this report.

Contents

Figures

Tables

Conversion Factors

U.S. customary units to International System of Units

Multiply	By	To obtain
	Length	
inch (in.)	2.54	centimeter (cm)
inch (in.)	25.4	millimeter (mm)
foot (ft)	0.3048	meter (m)
mile (mi)	1.609	kilometer (km)
mile, nautical (nmi)	1.852	kilometer (km)
yard (yd)	0.9144	meter (m)

International System of Units to U.S. customary units

Multiply	By	To obtain
	Length	
centimeter (cm)	0.3937	inch (in.)
millimeter (mm)	0.03937	inch (in.)
meter (m)	3.281	foot (ft)
kilometer (km)	0.6214	mile (mi)
kilometer (km)	0.5400	mile, nautical (nmi)
meter (m)	1.094	yard (yd)
	Mass	
gram (g)	0.03527	ounce, avoirdupois (oz)

Abbreviations

°C	degrees Celsius
CI	confidence interval
g/µg	grams per microgram
km	kilometer
$MgCO_3$	magnesium carbonate or magnesite
Ma	million years ago
m	meter
mg	milligram
µg	micrograms
µg/g	micrograms per gram
ml	milliliter
N	normal
n.d.	not determined
rpm	revolutions per minute
SBMNH	Santa Barbara Museum of Natural History
SD	standard deviation
2SD	2× standard deviation
Sr	strontium
USGS	U.S. Geological Survey
XRD	X-ray diffraction

Strontium Isotope Chronostratigraphic Age of a Sirenian Fossil Site on Santa Rosa Island, Channel Islands National Park, California

By James B. Paces[1], Scott A. Minor[1], Kevin M. Schmidt[1], and Jonathan Hoffmann[2]

Abstract

Fossils in the order Sirenia (family Dugongidae) from Santa Rosa Island, part of Channel Islands National Park in southern California, provide rare temporal and spatial links between earlier and later evolutionary forms of dugongids, and add information about their dispersal into the northeastern Pacific region. Marine sedimentary rocks containing these fossils have characteristics of both the late Oligocene to middle Miocene Vaqueros Sandstone and the early to middle Miocene Rincon formation observed elsewhere. To determine a more precise age of the fossils, marine invertebrate shells were collected from the same exposures as the sirenian fossils for chronostratigraphic assessment using strontium isotope compositions and the well-calibrated seawater strontium evolution curve. Shells used for analysis were from bivalve mollusks (*Pycnodonte* sp. [oyster] and *Lyropecten* sp. [scallop]) and crustaceans (*Balanus* sp. [barnacle]). Results show a wide range of $^{87}Sr/^{86}Sr$ values, indicating that shell materials experienced varying degrees of diagenetic alteration. Strontium concentrations and $^{87}Sr/^{86}Sr$ values in subsamples of *Pycnodonte* shell show correlations between original shell material and a secondary component having lower strontium concentrations and less radiogenic (lower) $^{87}Sr/^{86}Sr$. In contrast, all *Lyropecten* shell analyses yielded a uniform $^{87}Sr/^{86}Sr$ value (0.708440±0.000010 [2× standard deviation]) over a wide range of strontium concentrations (around 900 to 1,800 micrograms per gram [µg/g]). Results for *Balanus* shell subsamples show a range of strontium compositional behavior between the other two types of shell. Acetic acid leachates of sandy matrix confirm that diagenetic fluids had low $^{87}Sr/^{86}Sr$ values consistent with the least radiogenic values in *Pycnodonte* subsamples. A simple mixing model between two calcite end-members can explain observed *Pycnodonte* data, although actual diagenetic processes likely involved secondary dissolution/reprecipitation or strontium ion exchange between shell material and pore fluid. Data indicate that only *Lyropecten* subsamples have retained their original $^{87}Sr/^{86}Sr$ compositions, resulting in a best-estimate age of 20.08±0.11 million years ago (Ma) (±95-percent confidence interval [CI]). Although Dugongidae fossils have been found in Miocene and younger sediments along the west coast of North America, the Santa Rosa Island specimens represent some of the earliest and most accurately dated sirenian fossils in the region. Chronostratigraphic results also constrain the timing of the transgressional processes represented by shallow-water (Vaqueros Sandstone) to deep-water (Rincon formation) depositional environments.

Introduction

Sirenia, commonly known as sea cows, are an order of fully aquatic herbivorous mammals that evolved from land-based quadrupeds beginning in the early Eocene. The order diversified rapidly throughout the Eocene, Oligocene, and Miocene, and spread along the coasts of the shallow tropical seas during this time (Domning, 2018). Sirenians most likely reached the north Pacific region from the Caribbean via the Central American seaway by early- to middle-Miocene time (equivalent to the Hemingfordian North American land-mammal age of approximately 20 to 16 million years ago (Ma); Domning, 1978), although evidence for an earlier (late Oligocene to early Miocene) presence has been noted (Domning and Ray, 1986). Closure of the Central American seaway by as early as 15 Ma (Coates and others, 2004; Montes and others, 2015) resulted in isolation of Pacific and Atlantic populations of sirenians that continued to evolve separately. By the middle Miocene (equivalent to the Barstovian North American land-mammal age of 16.3 to 13.6 Ma; Alroy, 2000), at least three lineages in the Dugongidae family were present along the central west coast of North America, occupying different ecological habitats (Aranda-Manteca and others, 1994). At present, *Dugong dugon*, which inhabits the tropical waters of the Indo-Pacific, is the sole living species remaining in the once-diverse Dugongidae family after the cold-adapted *Hydrodamalis gigas* (Stellar's sea cow) that was endemic to the north Pacific, went extinct around 1768 C.E. (Domning, 2018). Although sirenian fossils from the eastern

[1]U.S. Geological Survey.

[2]Santa Barbara Museum of Natural History.

Pacific region indicate substantial diversity in the Neogene, the earliest records of sirenian dispersal and evolution in this region during the late Oligocene or early Miocene remain poorly documented.

Channel Islands National Park, consisting of San Miguel, Santa Rosa, Santa Cruz, Anacapa, and Santa Barbara Islands offshore of southern California (fig. 1*A*), contains a paleontological trove that includes marine invertebrates and vertebrates preserved in Cenozoic sedimentary strata. In 2012 and 2017, fossil remains of two sirenians (dugongids) were discovered by U.S. Geological Survey (USGS) geologists (coauthors Minor and Schmidt) while conducting geologic mapping and related investigations in the south-central uplifted fault block on Santa Rosa Island (fig. 1*B*). In 2018, paleontologists from the Santa Barbara Museum of Natural History (SBMNH; led by coauthor Hoffmann) stabilized and removed the more-recently discovered (2017) specimen (National Park Service task agreement P18AC00955 to Jonathan Hoffman) in order to to determine its taxonomic identity and paleoecologic context.

The fossil sirenian bones were found in a moderately well-exposed section of marine sandstones, siltstones, and mudstones previously mapped as either upper Vaqueros Sandstone (Weaver and others, 1969) or Rincon formation (Dibblee and others, 1998). On the coastal mainland north of Santa Rosa Island, the Vaqueros Sandstone was variously mapped as the Vaqueros Sandstone (Dibblee, 1986) or Vaqueros Formation (Minor and others, 2009), and the Rincon formation was mapped as the Rincon Shale (Dibblee, 1986; Minor and others, 2009). To avoid confusion in nomenclature, we use the local map unit names (Vaqueros Sandstone and Rincon formation) of Dibblee and others (1998) when referring to corresponding strata on Santa Rosa Island and mainland California.

The basal Vaqueros Sandstone principally consists of sandstone and represents a period of marine transgression. The age of the Vaqueros Sandstone was determined on mainland California near San Luis Obispo as 26.4±1.0 to 24.9±1.0 Ma based on seawater strontium-isotope correlation of scallop and oyster shell fragments from the northern Santa Maria Province in central California (Keller and others, 1996). Using similar strontium isotope methods, Rigsby (1998) reported an apparent age of the Vaqueros Sandstone ranging from 25 to 18 Ma in the Santa Ynez Mountains north of the Channel Islands, indicating that deposition there occurred from late Oligocene to early Miocene. The age of the overlying Rincon formation has been assigned as early Miocene (Saucesian benthic foraminiferal stage of Kleinpell [1938, 1980]) based on benthic and planktic foraminifera and calcareous nannofossils (Stanley and others, 1992). Given previous age estimates, a preliminary age of approximately 25 to 20 Ma was ascribed to the Santa Rosa Island sirenian fossils (National Park Service, 2018). Following deposition of the marine strata containing the sirenian fossils, the stratigraphic sequence was subjected to an unknown amount of burial, diagenesis, uplift, and exhumation, with vertical movement driven largely by tectonic forces. Strontium isotope chronostratigraphic methods similar to those employed here were used to estimate ages of elevated, wave-cut marine terraces on nearby Santa Cruz Island (Muhs and others, 2021) and on Santa Rosa Island (Muhs and others, 2023) in studies investigating the Pliocene to Pleistocene sea-level fluctuations and geomorphic histories of the Channel Islands.

The purpose of this study is to determine a more precise age for the geologic strata hosting the sirenian fossils using marine bivalve and barnacle fossils from the same sedimentary horizons hosting the fossil dugongids, and from beds between those horizons. Knowledge of a more precise age for these specimens is important because sirenian fossils are not well-represented from this period in the eastern Pacific (National Park Service, 2018), and because the late Oligocene to early Miocene age estimates indicate that the Santa Rosa Island sirenians could represent some of the earliest ancestors of sirenian lineages in the region (Domning, 1978; Domning and Ray, 1986; Aranda-Manteca and others, 1994). Furthermore, dating the site will help refine the paleolatitude of the original depositional site prior to its northwesterly tectonic translocation during and after the Miocene (Atwater, 1998); an important component to understanding paleobiogeographic distribution of sirenians.

Rather than direct radiometric dating of the sirenian fossils, we analyzed the strontium isotopic composition ($^{87}Sr/^{86}Sr$) of fossilized marine invertebrate shell material found in close stratigraphic and spatial proximity to the sirenian fossils. If the fossil shell material has remained unmodified since its formation, then the $^{87}Sr/^{86}Sr$ composition of these shells can be compared with known variations of seawater $^{87}Sr/^{86}Sr$ that have been precisely calibrated with time throughout the Miocene (McArthur and others, 2001; 2020). However, poorly constrained secondary geochemical processes involving diagenetic alteration can complicate simple interpretation of strontium isotope data because of elemental gains, losses, or exchanges. We utilize analyses of strontium concentrations and $^{87}Sr/^{86}Sr$ values from numerous specimens to identify materials that may have experienced diagenetic alteration or contamination with secondary strontium derived from the host sediment. Once compromised analyses are rejected, a precise and accurate age estimate can be determined based on the original, seawater-derived strontium preserved in unaltered shells.

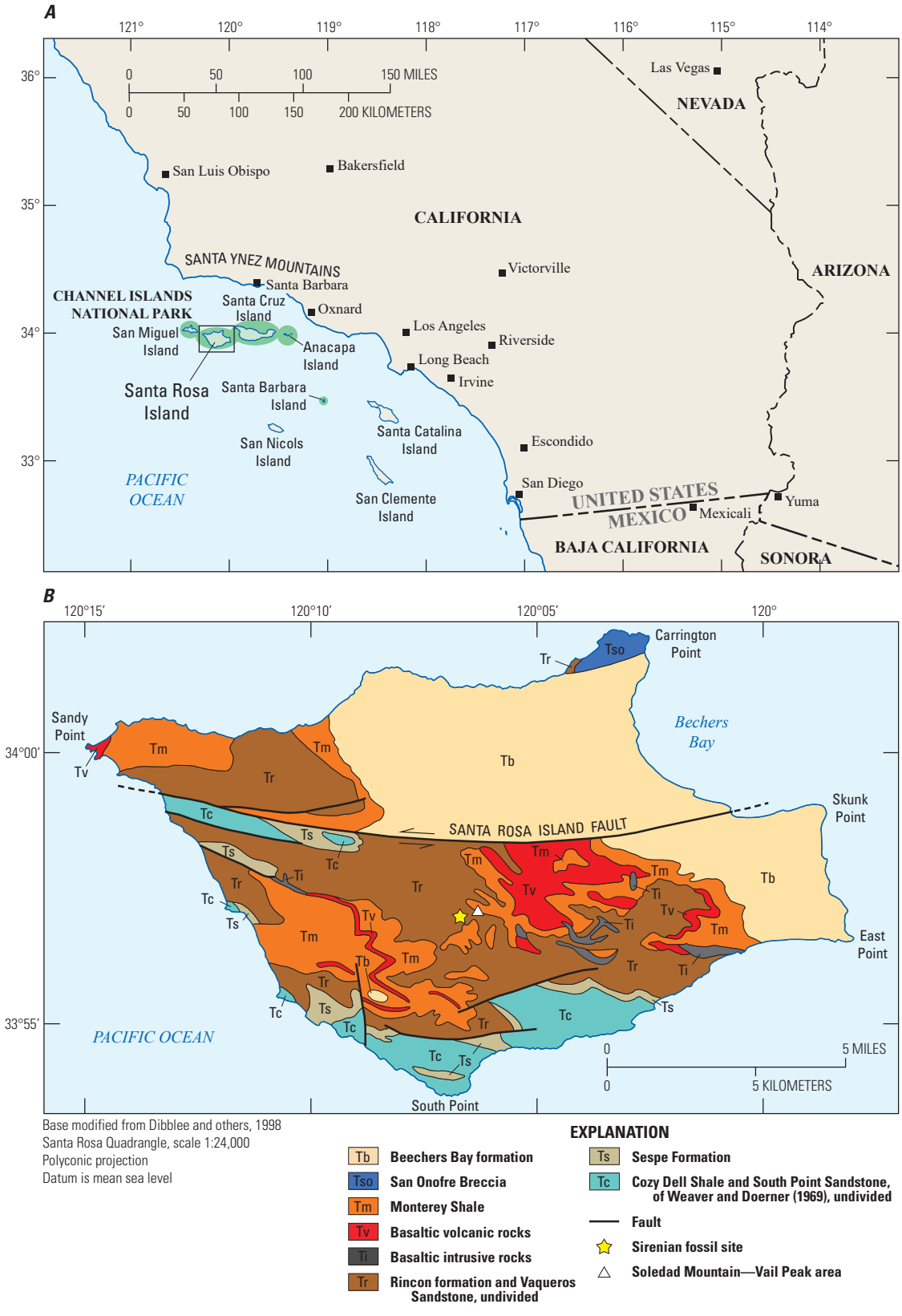

Figure 1. Location map of the Channel Islands National Park (*A*) and simplified geologic map (*B*) of Santa Rosa Island, California, showing the location of the sirenian fossils contained in rocks mapped as Rincon formation by Dibblee and others (1998) and Vaqueros Sandstone by Weaver and others (1969). Geologic map is modified from Dibblee and others (1998), with stratigraphic nomenclature adopted from that same source.

Geologic Context

The bedrock of Santa Rosa Island mostly consists of Eocene through Miocene marine sedimentary rocks (Weaver and others, 1969; Dibblee and Ehrenspeck, 1998; Dibblee and others, 1998) (fig. 1*B*). A temporary pause in this marine depositional sequence is represented by late Oligocene terrestrial sedimentary rocks of the Sespe Formation. In addition, Miocene volcanic rocks and associated shallow-intrusive rocks are present, mainly on the southern part of the island. The oldest rocks (Eocene and Oligocene) are exposed mainly on the southern and western parts of Santa Rosa Island, and strata become progressively younger towards the east and north across much of the island. Locally, gentle, open folds and faults with moderate (tens to hundreds of meters) displacement and various types of movement deform the strata. The dominant structural element of Santa Rosa Island is the east–west-striking Santa Rosa Island Fault (fig. 1*B*). This fault spans the island, and separates the more mountainous, elevated, and dissected southern half of Santa Rosa Island from the less elevated tablelands and uplands of the island's northern half (Minor and others, 2012). The Santa Rosa Island Fault has experienced a protracted history of late Cenozoic movement, including Miocene normal slip that uplifted the southern part of the island, and Quaternary sinistral strike slip and reverse slip.

The sirenian fossils were found eroding from the walls of a steep ravine and cliff-face approximately 400 meters (m) above modern sea level in the more rugged and dissected south-central part of the island (fig. 2). Nearby Soledad Mountain (480 m) and Vail Peak (484 m), the highest peaks on the island, form part of a ridge crest above the fossil-bearing cliff exposures. The gently dipping sedimentary stratigraphic section underlying the ridge consists predominantly of marine mudstones, siltstones, and sandstones (fig. 2). A conspicuous normal fault displaces the section downward by an undetermined amount just south of the fossil site. Precise coordinates of the site are not given in this report by request of the National Park Service in order to protect sensitive paleontological resources under their jurisdiction.

The stratigraphically lower sirenian fossil, discovered in 2017 and extracted in 2018, was located near the top of an approximately 1–2 m-thick sandy pebble-conglomerate layer at the base of the exposed section just a few meters north of the normal fault trace (horizon 1 in fig. 2). The conglomerate is moderately cemented with calcium carbonate and contains marine invertebrate fossils (*Balanus* sample SBMNH-VP-2019). About 4.5 m of poorly exposed mudstone and siltstone overlie the conglomerate. Those mudstone and siltstone layers are overlain by a fine-grained, bioturbated sandstone layer (horizon 2 in fig. 2) containing marine invertebrate fossils (*Pycnodonte* and *Lyropecten* samples SRI-18009). Overlying the bioturbated sandstone layer is a poorly exposed interval of mudstone and siltstone that includes a small exposure approximately 1 m above its base (horizon 3 in fig. 2) containing marine invertebrate fossils (*Balanus* sample SBMNH-VP-2051 and *Lyropecten* sample SBMNH-VP-2055).

The stratigraphically higher sirenian fossil horizon discovered in 2012 is located northeast of the three fossil shell sample sites noted above, and north of a prominent ravine (horizon 4 in fig. 2). The sirenian fossil specimen was eroding from a silty, fine-grained sandstone interval (see inset photo in fig. 2) that contains abundant marine invertebrate fossils (*Lyropecten* sample SBMNH-VP-2026 and *Balanus* sample SBMNH-VP-2031). This sandstone layer can be traced south across the ravine to an exposure directly above where the lower sirenian specimen was extracted in 2017, and where invertebrate fossils were sampled from units adjacent to and overlying that specimen (horizons 1, 2, and 3 in fig. 2). A thicker and more prominent sandstone interval exposed below the original sirenian-bearing sandstone can also be traced southward across the ravine, lending support to the traced position of the upper sandstone, indicated by the uppermost "ss" label in the central part of figure 2. Additional mudstone and siltstone underlie the soil- and colluvium-covered slopes above those two sandstone intervals. Based on the elevation of the projected sandstone layer, we estimate that approximately 13 m of stratigraphic section separates the upper and lower sirenian horizons (stratigraphic horizons 4 and 1, respectively, in fig. 2).

A lingering question since publication of the first geologic map of Santa Rosa Island (Weaver and others, 1969) is which formation (or formations) constitutes the sedimentary sequence that forms the Soledad Mountain/Vail Peak ridge and includes the sirenian fossils? Specifically, it is not clear whether the fossil-bearing rocks belong to the upper part of the Vaqueros Sandstone as mapped by Weaver and others (1969), or the Rincon formation as mapped by Dibblee and others (1998). Some aspects of the sirenian-bearing unit, such as fossiliferous, bioturbated sandstone intervals, and local pebble conglomerates, closely resemble the Vaqueros Sandstone as mapped and described in the Santa Ynez Mountains (Dibblee, 1982; Rigsby, 1998) and Santa Barbara coastal plain (Minor and others, 2009) of mainland California. Other sedimentary characteristics, such as thick mudstone and siltstone intervals, more closely resemble the Rincon formation as mapped on the mainland. However, the most diagnostic features characterizing each of these formations on the coastal California mainland are absent in the Santa Rosa Island sirenian-bearing section. The Santa Rosa Island section lacks thick (tens of meters), uninterrupted intervals of fissile shale and claystone, commonly containing dolomitic concretions, that are observed elsewhere in the Rincon formation (Minor and others, 2009). Furthermore, the thick, massive, continuous sandstone beds and intervals typical of the Vaqueros Sandstone on the mainland are not present in Santa Rosa Island exposures. Based on the observed lithostratigraphy, we interpret the sirenian section as part of a regional marine lithofacies transition between deposits consisting of shallow-water, coarse sediment

(Vaqueros Sandstone) and deposits consisting of deep-water, fine sediment (Rincon formation). Woolley (1998) suggested that parts of the Rincon formation on Santa Rosa Island may be a fine-grained lithofacies of the Vaqueros Sandstone. The geochronologic data reported here provide some constraints on the timing of deposition of this facies transition.

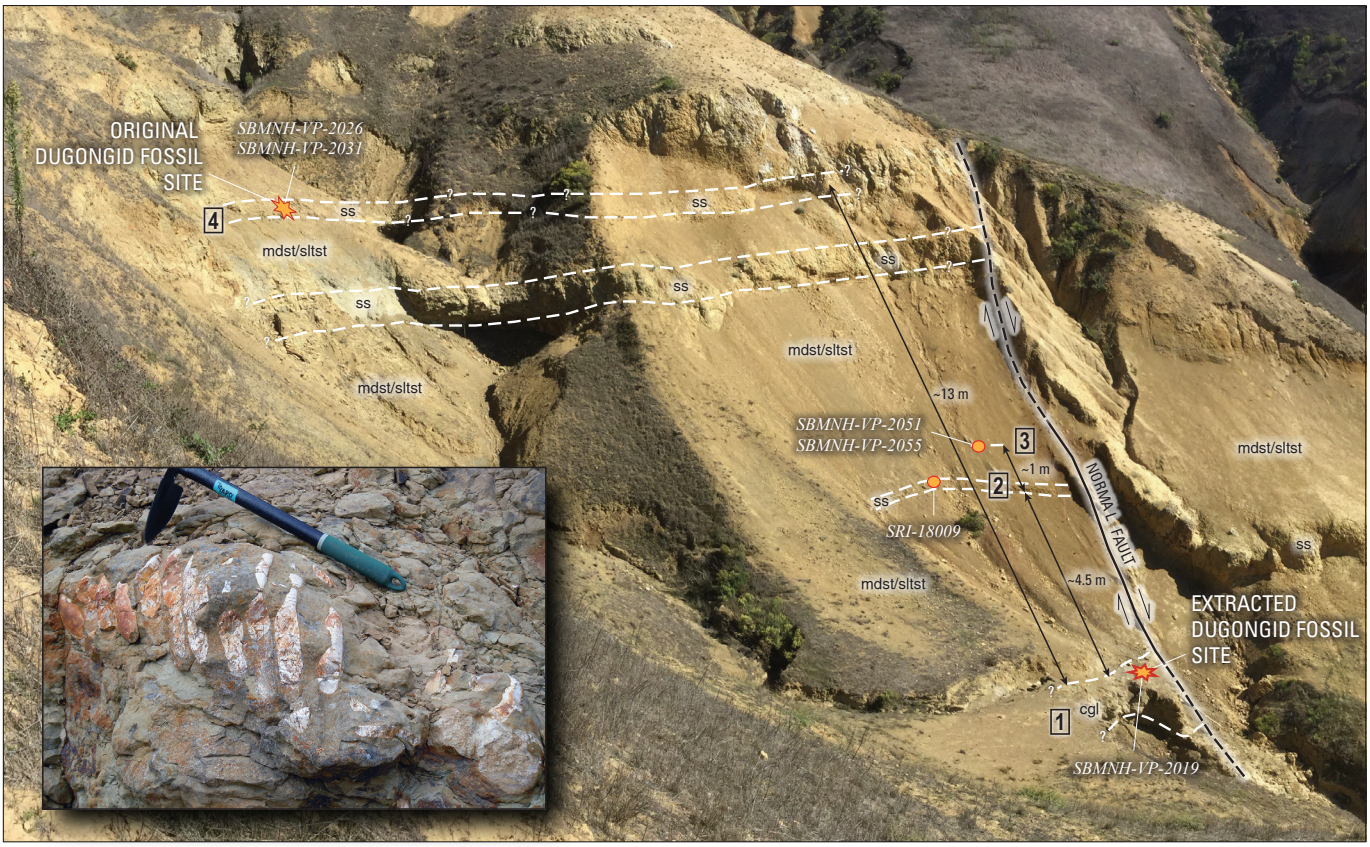

Figure 2. Oblique photograph looking east towards the hillside site where sirenian (dugongid) fossils were discovered. The stratigraphic relations of sedimentary layers containing marine invertebrate fossils collected for strontium isotope chronostratigraphic dating (sample identifiers are in italics) are visible. The hillside exposes a sequence of marine sandstone (ss), mudstone and siltstone (mdst/sltst), and conglomerate (cgl) layers. Measurements between sampled horizons approximate true stratigraphic thickness in meters (m). Numbers in rectangles refer to the stratigraphic horizon identifiers used in table 1. Inset shows a partial ribcage of the original dugongid fossil as it was found in 2012. The pick lying above the exposed bones has a 0.4-m-long handle.

Samples

The taxonomic assignments of mollusk and barnacle fossils collected by USGS and SBMNH personnel between 2017 and 2020 were determined at the SBMNH. Macroscopic shells included individual specimens or fragments of *Pycnodonte* sp. (extinct oysters), *Lyropecten* sp. (scallops), and *Balanus* sp. (barnacles). Most shells collected from outcrops were embedded in a well-cemented, gray-to-brown, fine-grained matrix of sandstone and siltstone.

Marine organisms that precipitate calcium carbonate shell material incorporate Sr^{2+} dissolved in seawater at the time of formation; therefore, shells of multiple, stratigraphically related specimens are expected to contain uniform $^{87}Sr/^{86}Sr$ values if postdepositional diagenetic alteration is not a factor. To assist in subsampling for strontium isotope analyses, individual shells or shell fragments were cut into slabs and polished to reveal cross-sections showing internal textures. Large *Pycnodonte* sp. shells commonly include a variety of internal structures and fabrics, such as uniform, dark-gray micrite; finely laminated micrite; areas of coarse, palisade-like crystal structures; and zones of buff shell with alternating coarse- and fine-grained crystal textures (figs. 3 and 4). Those textural variations are similar to primary fabrics present in modern oyster shells (see figure 68 of Taylor and others, 1969). Multiple textural variants occurring in several of the larger individual specimens of *Pycnodonte* (SRI-18009A-1A, -1B, -2A, and -3A) were specifically targeted to assess the uniformity of strontium isotopic compositions (fig. 3).

Specimens of *Lyropecten* sp. were generally well-preserved with dense, homogeneous, dark-gray, microlaminated shell walls (fig. 5). Sections of ribbed walls have uniform thicknesses without clear distinction between inner and outer structures (fig. 5*D*). In addition to several whole valves, smaller separate fragments were obtained from the upper sirenian-bearing sandstone layer (SBMNH-VP-2026 from stratigraphic horizon 4 in fig. 2) as well as the underlying mudstone and sandstone layers (SBMNH-VP-2055 from stratigraphic horizon 3; SRI-18009 from stratigraphic horizon 2). One whole shell was subsampled twice (SBMNH-VP-2055 and SBMNH-VP-2055.v2) from different areas to test reproducibility of $^{87}Sr/^{86}Sr$ values from a single *Lyropecten* sp. specimen.

Specimens of *Balanus* sp. consisted of plates forming whole carapaces, or disaggregated plate fragments (fig. 6) that preserved internal anatomical structures similar to those described in modern barnacle shell walls (Checa and others, 2020). In particular, outer halves of barnacle plate walls contain longitudinal cavities (canals) and intervening septa that result in significant primary porosity. The inner halves of barnacle plate walls consist of dense calcite formed by intergrowth of the primary septa, creating convoluted growth laminae referred to as interlaminate figure. In fossil barnacle-plate specimens, pores in the outer plate walls are now filled with fine detrital sediment or coarsely crystalline calcite. In contrast, inner plate walls still have low primary porosity and delicate primary growth fabrics, indicating minimal secondary recrystallization. Initial subsampling (termed phase 1) incorporated entire plate walls that included both longitudinal canal and interlaminate figure materials. Subsequent subsampling (termed phase 2) specifically targeted nonporous inner-plate walls with dense, interlaminate figure as shown by yellow outline in figure 6*D*.

Subsamples from larger shells or shell fragments were obtained using carbide dental drills to excavate micro-trenches or pits in broad areas of uniform texture. For thinner walled materials, exterior and interior surfaces were removed using a carbide drill-bit until only the core of the shell wall remained. Fragments cleaned in this manner were pulverized using an alumina mortar and pestle. The resulting powdered material was used for X-ray diffraction, strontium concentration determination by isotope dilution, and $^{87}Sr/^{86}Sr$ analysis by thermal-ionization mass spectrometry.

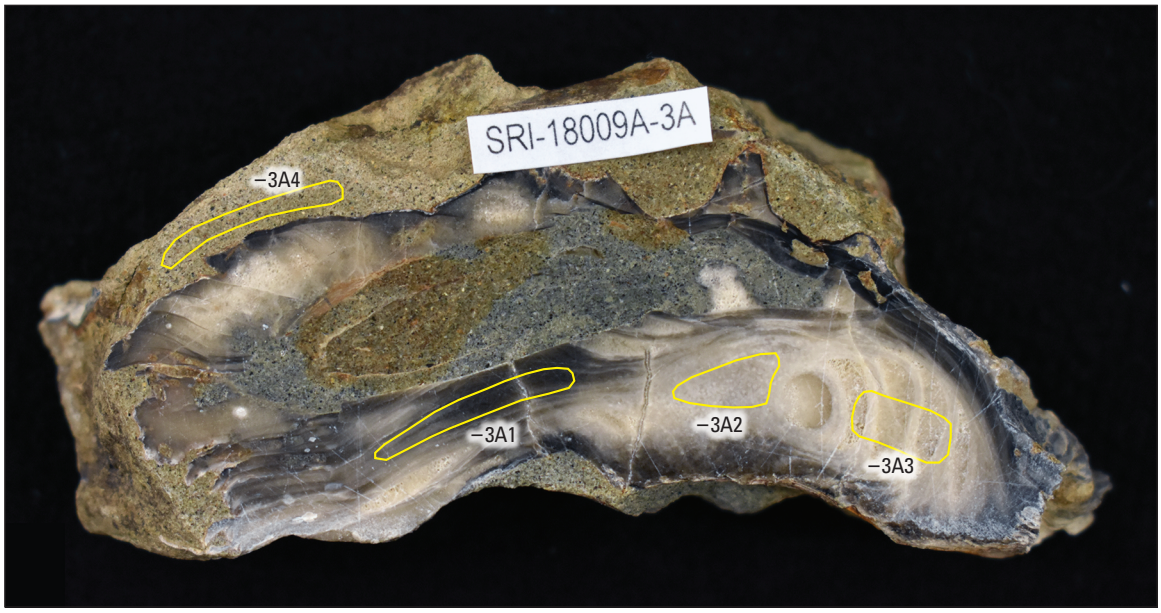

Figure 3. Photograph of a polished slab of sandstone containing a large fossil *Pycnodonte* sp. (oyster) shell in cross-section. Yellow polygons enclose areas of shell that were subsampled for strontium isotope analyses (SRI-18009A-3A1, -3A2, and -3A3), and one area of sandstone matrix subsampled to evaluate the isotopic composition of postdepositional calcite cement (SRI-18009A-3A4). White label is approximately 17 millimeters in length.

Figure 4. Photograph of a polished section of a *Pycnodonte* sp. (oyster) shell fragment showing complex textural relations, including gray, finely laminated micrite and lenses of coarse, palisade-like crystals. Yellow polygon encloses area where material was subsampled for strontium isotope analyses (SRI-18009A-3B1). mm, millimeters.

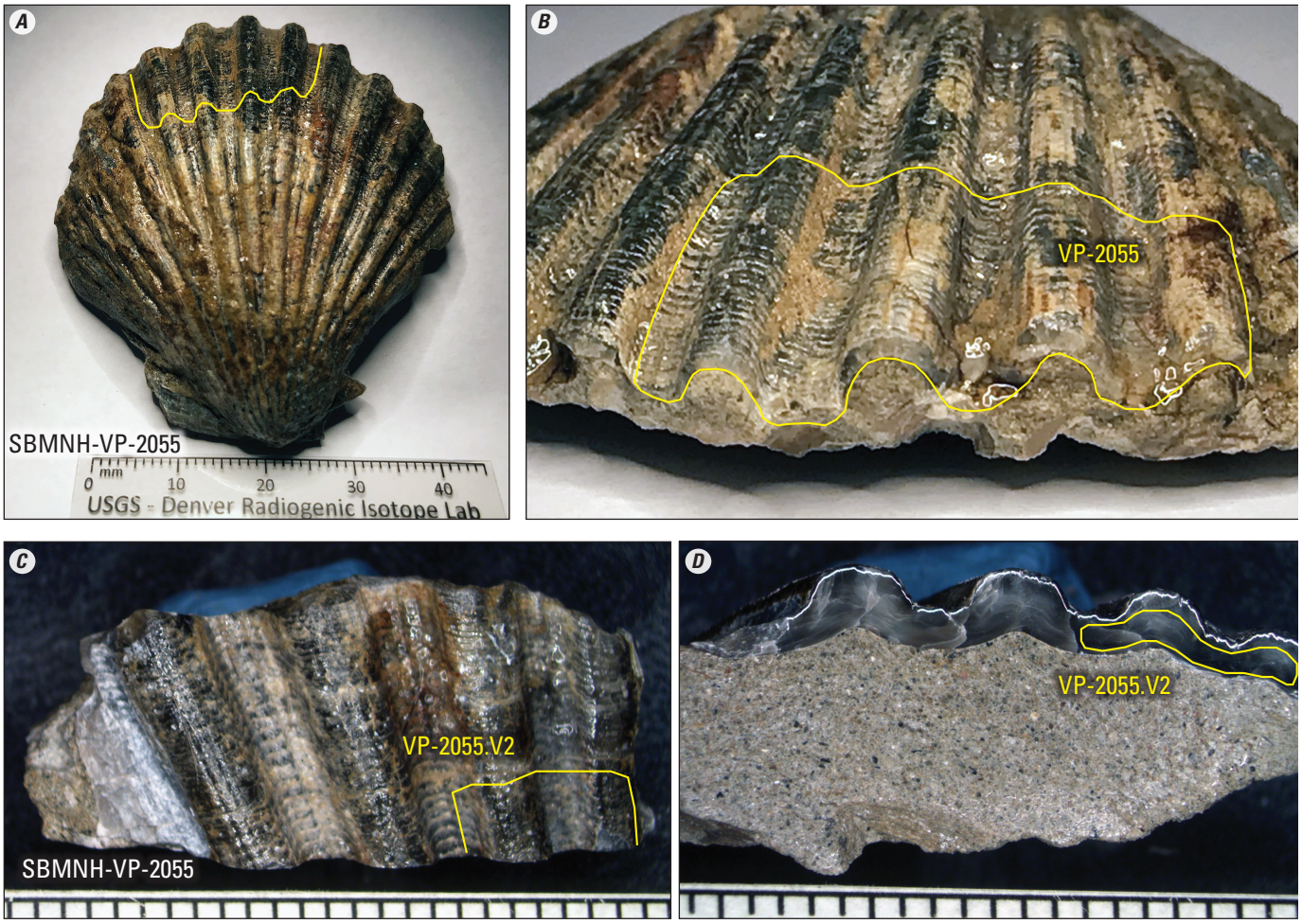

Figure 5. Photographs of fossil *Lyropecten* sp. (scallop) shell used for strontium isotope analyses. *A* is a whole shell; *B* is oblique view of the same shell (upper left side in *A*) with yellow polygon showing area subsampled as SBMNH-VP-2055 after grinding away exterior surface, prying shell off of the underlying sandy matrix, and cleaning of the interior surface. *C* is a separate fragment of the same shell (lower left side in *A*), with yellow outline showing area subsampled as SBMNH-VP-2055.v2. *D* shows a polished cross-section showing internal shell texture, with subsampled area outlined in yellow. Tick marks at the bottom of photos *C* and *D* are millimeters. mm, millimeters.

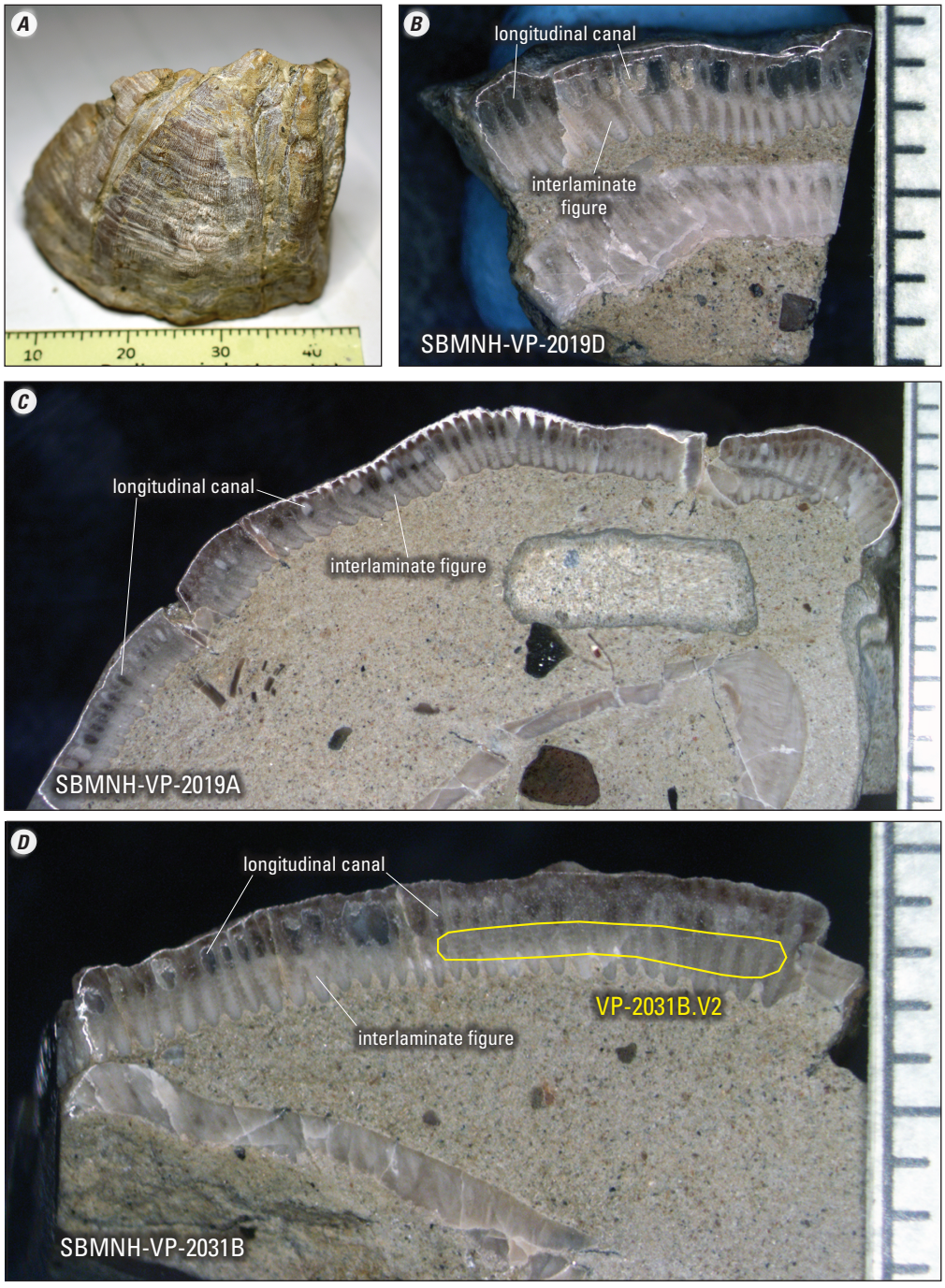

Figure 6. Photographs of fossil *Balanus* sp. (barnacle) shells used for strontium isotope analyses. *A* is a whole specimen (sample SBMNH-VP-2019A) showing multiple plates that form a nearly complete carapace. Tick marks on scale are millimeters. Photographs *B*, *C*, and *D* are polished cross-sections of several plate walls surrounding a fine sand matrix that fills the interiors. The outer half of plate walls contain longitudinal canals now filled with silty sediment or secondary calcite. The inner half of plate walls consist of interlaminate figure—delicate growth structures formed by primary septa that coalesce during growth. Phase 1 subsamples included the entire plate wall (longitudinal canal plus interlaminate figure), whereas phase 2 subsamples specifically targeted interlaminate figure as shown by yellow outline in *D*. Tick marks on the right sides of photographs *B*, *C*, and *D* represent millimeters.

Analytical Methods

X-Ray Diffraction

Carbonate mineralogy (aragonite, high-magnesium calcite, low-magnesium calcite) of a subset of shell samples was determined using standard X-ray diffraction (XRD) techniques (for example, Moore and Reynolds, 1989) at USGS laboratories in Denver, Colorado. Approximately 100 milligrams (mg) of powdered material were packed into an aluminum holder and scanned from 20 to 35° 2-theta (θ) at 2° 2θ per minute using nickel-filtered, Cu-Kα radiation generated at 45 kilovolts and 30 milliamperes. The mole-percent magnesium carbonate ($MgCO_3$) content in calcite of the fossil specimens was determined by measuring the shift in the position of the main 2θ peak for pure calcite at 29.42° to higher values (Chave, 1952; Goldsmith and others, 1955). The change in 2θ angle (Δ2θ) was compared to an empirical calibration curve determined for calcite specimens with known magnesium contents. Calibration results indicate that Δ2θ values are linearly correlated with $MgCO_3$ contents in calcite between about 1.5 and 18 mole-percent ($r^2 = 0.98$). Uncertainties for XRD results are estimated to be better than ±2 mole-percent of the value thus obtained.

Strontium Isotope Analysis

All sample preparation, processing, and analyses for strontium concentrations and isotopic compositions were performed at USGS Denver Radiogenic Isotope Lab facilities. Aliquots of 10–30 mg of powdered shell material were weighed into two separate Teflon vials for each sample. Smaller aliquots used for strontium concentration by isotope dilution were digested with high-purity 7 normal (*N*) nitric acid, spiked with known weights of ^{84}Sr-enriched tracer solution, and allowed to equilibrate overnight on a 90 degrees Celsius (°C) hotplate. Samples were transferred to 2 milliliter (ml) centrifuge tubes and spun at 10,000 revolutions per minute (rpm) for 10 minutes. The supernatant was transferred to the original Teflon vial, and any residue was washed several times with deionized water, transferred to a new, weighed centrifuge tube, dried, and reweighed to calculate the percentage of carbonate. Larger, unspiked aliquots used for $^{87}Sr/^{86}Sr$ analysis were leached overnight in 5 *N* acetic acid at room temperature. Resulting solutions were transferred to 2 ml centrifuge tubes and spun at 10,000 rpm for 10 minutes. The supernatant was transferred back to the original Teflon vial and any residue was discarded. Acetic acid solutions were evaporated to dryness, redissolved in high-purity concentrated nitric acid, dried again, and redissolved in 7 *N* nitric acid. Strontium separates for both spiked and unspiked samples were purified by ion chromatography following procedures described elsewhere (De Muynck and others; 2009; Paces and others, 2020) using Eichrom Sr Resin.

Isotope measurements were made using a Thermo-Finnigan Triton multi-cup thermal-ionization mass spectrometer fitted with a single electron multiplier for ion counting. Purified strontium salts were loaded on single rhenium filaments that had been doped with a small amount of tantalum-chloride activator solution. Values of $^{84}Sr/^{86}Sr$ were determined on spiked aliquots using a single MasCom discrete-dynode electron multiplier operating in peak jumping mode, and the resulting values were used to determine strontium concentrations using isotope dilution calculations (Faure and Mensing, 2005). Precision and accuracy of concentration determinations are better than 1 percent as estimated by monitoring interlaboratory comparison samples distributed as part of the Standard Reference Sample program administered by the USGS Branch of Quality Systems (https://bqs.usgs.gov/srs/).

$^{87}Sr/^{86}Sr$ compositions determined from unspiked aliquots were analyzed on the same instrument using loads of about 0.5 micrograms (µg) of strontium that typically yielded approximately 6 volt or larger ^{88}Sr signals. A triple-jump, multidynamic peak-hopping routine was used to collect three $^{87}Sr/^{86}Sr$ ratios per scan to counter any biases that may exist between individual Faraday cups. Raw $^{87}Sr/^{86}Sr$ ratios were normalized for mass fractionation using the same factor required to adjust the measured value of $^{86}Sr/^{88}Sr$ to the accepted value of 0.11940. The presence of rubidium was monitored and used to correct ^{87}Sr, although ^{85}Rb was functionally absent.

Data for $^{84}Sr/^{86}Sr$ were also monitored to ensure the effectiveness of the fractionation correction. A resulting value of 0.056499±0.000008 (±2× standard deviation, or 2SD) was obtained for 272 runs of the National Institute of Standards and Technology strontium carbonate standard reference material 987 analyzed between 2016 and 2021. Total-process blank contributions are between 40 and 100 picograms of strontium. The mean $^{87}Sr/^{86}Sr$ value obtained for 263 analyses of SRM987 collected over the same 5-year period was 0.710251±0.000007 (2SD), which is within uncertainty of the accepted value of 0.710248±0.000006 (McArthur and others, 2001). Final uncertainties for $^{87}Sr/^{86}Sr$ determinations include both internal (counting statistics based on individual analyses) and external (precision of multiple SRM987 analyses) sources of error added in quadrature, and are given at the 95-percent confidence level. In order to correct for instrument bias, $^{87}Sr/^{86}Sr$ values determined for unknown samples were normalized by the same factor required to adjust the average $^{87}Sr/^{86}Sr$ obtained for SRM987 standards included in each sample magazine to the accepted value given above. A secondary USGS strontium isotope standard (EN-1) derived from a modern giant clam shell (*Tridacna* sp.) from Enewetak Atoll (Ludwig and others, 1988) was analyzed as an unknown with each batch of samples. 195 analyses determined over the same 5-year period yielded a mean normalized $^{87}Sr/^{86}Sr$ value of 0.709173±0.000009 (2SD), which is nearly identical to the accepted value of 0.709174±0.000002 (±2× standard error; McArthur and others, 2006; 2020).

Results and Discussion

Carbonate Mineralogy

Carbonate-forming marine organisms utilize biomineralization pathways to construct shells from undersaturated ionic solutions that normally would not support carbonate precipitation (Pérez-Huerta and others, 2018). Biomineralization strategies typically use organic proteins or high magnesium concentrations to stabilize amorphous calcium carbonate, either as aragonite or high-magnesium calcite. Modern oyster and scallop shells mostly are made of calcite and can also include smaller amounts of aragonite, whereas shells of modern barnacles, including extant species of *Balanus*, are constructed wholly of calcite (Milliman, 1974). Both high-magnesium calcite and aragonite are thermodynamically unstable under surface conditions, but these minerals are common products of biogenically produced carbonate shells (Pérez-Huerta and others, 2018). Unstable phases of calcium carbonate commonly revert to more stable, low-magnesium calcite during diagenesis.

Mineralogical results determined by XRD for a subset of *Pycnodonte* and *Lyropecten* subsamples confirm that shells are composed of calcite, with magnesium contents ranging from 3.7 to 9.2 mole-percent $MgCO_3$ (table 1). Most analyses are above the 3–4 mole-percent threshold for biogenic high-magnesium calcite (Long and others, 2014; Pérez-Huerta and others, 2018). Concentrations of $MgCO_3$ show no correlation with strontium concentration for a given subsample texture or fossil type (fig. 7*B*). For three *Pycnodonte* specimens with multiple subsamples targeting distinct color and texture differences (SRI-18009A-1A, SRI-18009A-1B and SRI-18009A-3A), $MgCO_3$ contents are identical regardless of textural type (gray micrite; buff, coarse crystalline; mixed). One of the three subsamples from shell SRI-18009A-3A with a mixture of textures has a slightly lower $MgCO_3$ content (fig. 7*B*); however, that difference is likely within analytical error. None of the analyzed subsamples contained aragonite as identified by XRD data, indicating that if any aragonite had been present initially, it has been altered to calcite.

Strontium Concentrations

Biomineralization of calcium carbonate in marine organisms results in incorporation of relatively large amounts of Sr^{2+} from seawater because it substitutes readily for structural Ca^{2+} in primary shell material, especially in aragonite, where the larger Sr^{2+} ion is accommodated more readily in the orthorhombic mineral structure. However, any recrystallization caused by interactions with diagenetic solutions commonly involves loss of original strontium, especially if original aragonite or high-magnesium calcite is converted to low-magnesium calcite. Milliman (1974) listed ranges and means of strontium concentrations from the shells of modern organisms including oysters (*Ostrea*: 700–1,900 micrograms per gram (µg/g) with a mean of 1,300 µg/g), scallops (*Pecten*: 700–2,200 µg/g with a mean of 1,400 µg/g), and barnacles (*Balanus*: 700–6,000 µg/g with a mean of 2,900 µg/g). Therefore, fossil shells subject to diagenetic alteration will commonly have strontium concentrations lower than those values. Strontium concentrations have been used to evaluate the integrity of Cretaceous rudist (extinct bivalve mollusk) shells from the Caribbean (Bonilla-Rodríguez and others, 2014), where specimens with values >900 µg/g yielded uniform $^{87}Sr/^{86}Sr$ values when compared to specimens with concentrations <900 µg/g, which yielded lower $^{87}Sr/^{86}Sr$ values. Those authors demonstrated that strontium concentrations represent a sensitive indicator of how effectively strontium that was originally sequestered at the time of shell formation had been retained over millions of years.

Shell subsamples in this study have a wide range of strontium concentrations, between 163 and 2,410 µg/g (table 1; data available as downloadable files in Paces, 2022), that are dependent, in part, on genus type (fig. 7*A*). Strontium concentrations in *Pycnodonte* sp. shells are systematically lower (163–537 µg/g) than those in *Lyropecten* sp. (924–1,755 µg/g) and most *Balanus* sp. (1,061–2,410 µg/g except for two subsamples with 363 and 438 µg/g) specimens (table 1). Observed differences in strontium concentration might be caused by differences in the amounts of calcite versus aragonite originally present in a given shell. Oysters (*Pycnodonte*) and scallops (*Lyropecten*) construct shells that are mainly calcite with a relatively thin band of aragonite where soft tissue is attached to the shell (Taylor and others, 1969), and that aragonite is maintained as a separate, distinct layer throughout growth. Taylor and others (1969) also described the dominantly calcitic, foliated structures of oyster shells that are arranged approximately parallel to shell surfaces, with "chalky" layers (see fig. 68 of Taylor and others, 1969) consisting of lenses of vertically arranged, irregular calcite fibers intercalated between denser folia of laminated micrite, very much like the structures shown here in figures 3 and 4. Barnacle (*Balanus*) plates are constructed wholly of calcite with both rhombohedral and fibrous microstructures (Checa and others, 2020).

Strontium concentrations in *Pycnodonte* shells are further correlated with shell color and texture (figs. 3 and 4). Subsamples of buff, coarse-grained textures have the lowest strontium concentrations (163–269 µg/g), whereas subsamples consisting of darker gray, finely laminated textures, often from the same specimen, have moderate concentration values (360–537 µg/g). Subsamples of thinner, gray pectinid shells with massive to microlaminated micritic textures have strontium concentrations greater than 924 µg/g. Calcite samples from barnacle wall plates also have elevated strontium concentrations, with little difference between subsamples of whole shell walls (phase 1 samples with a mean and ±standard deviation (SD) of 1,454±491 µg/g) and subsamples restricted to dense interlaminate figure (phase 2 samples with a mean and ±SD of 1,551±424 µg/g). Similarities in concentration between the two sample sets indicate that the

strontium concentrations of any secondary calcite filling longitudinal canals is small relative to concentrations in primary biomineralized calcite.

Evaluation of secondary alteration in a suite of marine shell material can be enhanced by analyzing any closely associated diagenetic carbonate and altered fossil materials to help constrain the diagenetic trajectory in target specimens (Ullmann and Korte, 2015). We investigated the possibility of the presence of carbonate cements precipitated from diagenetic fluids by analyzing leachates of sediments that hosted the fossil shells. Readily dissolvable components for four of six samples of fine-grained sandy sediment ranged from 36 to 43 weight-percent, and are assumed to represent intergranular carbonate cement introduced during diagenesis. Two other matrix samples have higher carbonate contents (50 and 63 weight-percent), which may have been caused by inclusion of a carbonate clastic component. Concentrations of strontium in the leached carbonate components of matrix material (authigenic cement plus any clastic calcite) vary widely, from 44 to 906 µg/g, with an average of 457 µg/g and a median of 370 µg/g.

Table 1. Strontium concentrations, $^{87}Sr/^{86}Sr$ compositions and apparent seawater strontium ages for shells and matrix leachates from deposits associated with sirenian fossils, Santa Rosa Island, California.

[n.d., not determined; µg/g, micrograms per gram; Ma, million years ago]

Sample identifier	Sample type	Subsample description	Stratigraphic horizon*	Percent leachable fraction#	Mole percent $MgCO_3$ in calcite†	Strontium concentration (µg/g)‡	$^{87}Sr/^{86}Sr$	±2 sigma	Apparent seawater-strontium age (Ma)@
SRI-18009A-1A1	*Pycnodonte* sp.	Gray, laminated micrite	2	n.d.	7.1	361	0.708342	0.000009	21.6
SRI-18009A-1A2	*Pycnodonte* sp.	Buff, coarse crystalline	2	n.d.	7.1	269	0.708192	0.000010	24.1
SRI-18009A-1B1	*Pycnodonte* sp.	Gray, laminated micrite	2	n.d.	6.5	525	0.708402	0.000009	20.6
SRI-18009A-1B2	*Pycnodonte* sp.	Buff, coarse crystalline	2	n.d.	6.4	163	0.707911	0.000010	31.9
SRI-18009A-2A1	*Pycnodonte* sp.	Buff, coarse palisade	2	n.d.	6.4	170	0.708061	0.000009	26.7
SRI-18009A-3A1	*Pycnodonte* sp.	Gray, laminated micrite	2	n.d.	5.7	434	0.708375	0.000010	21.0
SRI-18009A-3A2	*Pycnodonte* sp.	Buff, coarse crystalline	2	n.d.	5.7	250	0.708248	0.000009	23.1
SRI-18009A-3A3	*Pycnodonte* sp.	Buff, mixed texture	2	n.d.	5.1	173	0.708030	0.000010	27.6
SRI-18009A-3B1	*Pycnodonte* sp.	Gray, laminated micrite	2	n.d.	3.7	360	0.708299	0.000009	22.3
SRI-18009A-3D1	*Pycnodonte* sp.	Gray, laminated micrite	2	n.d.	5.0	537	0.708395	0.000009	20.7
SRI-18009A-3E1	*Pycnodonte* sp.	Buff–gray, mixed texture	2	n.d.	5.4	375	0.708307	0.000009	22.1
SRI-18009A-4A1	*Pycnodonte* sp.	Buff, micritic, massive	2	n.d.	7.1	242	0.708238	0.000009	23.3
SRI-18009A-4D1	*Lyropecten* sp.	Gray micrite	2	n.d.	9.2	998	0.708434	0.000010	20.2
SRI-18009A-4E	*Lyropecten* sp.	Gray micrite	2	n.d.	n.d.	972	0.708441	0.000010	20.1
SRI-18009A-4F1	*Lyropecten* sp.	Gray micrite	2	n.d.	6.4	1064	0.708447	0.000010	20.0
SRI-18009A-4G	*Lyropecten* sp.	Gray micrite	2	n.d.	n.d.	1035	0.708442	0.000011	20.1
SRI-18009A-4H	*Lyropecten* sp.	Gray micrite	2	n.d.	n.d.	1094	0.708440	0.000009	20.1
SBMNH-VP-2026A	*Lyropecten* sp.	Gray micrite	4	98	n.d.	1366	0.708438	0.000009	20.1
SBMNH-VP-2055	*Lyropecten* sp.	Gray micrite	3	99	n.d.	1755	0.708444	0.000011	20.0
SBMNH-VP-2055.v2	*Lyropecten* sp.	Gray micrite	3	99	n.d.	1138	0.708444	0.000009	20.0
SBMNH-VP-2055A	*Lyropecten* sp.	Gray micrite	3	96	n.d.	924	0.708437	0.000009	20.1
SBMNH-VP-2055B	*Lyropecten* sp.	Gray micrite	3	93	n.d.	1240	0.708431	0.000010	20.2
SBMNH-VP-2019A	*Balanus* sp.	Whole shell wall	1	98	n.d.	438	0.708420	0.000011	20.4
SBMNH-VP-2019A1	*Balanus* sp.	Interlaminate figure	1	100	n.d.	1360	0.708402	0.000010	20.6
SBMNH-VP-2019A2	*Balanus* sp.	Interlaminate figure	1	96	n.d.	1473	0.708398	0.000009	20.7
SBMNH-VP-2019B	*Balanus* sp.	Whole shell wall	1	98	n.d.	363	0.708395	0.000009	20.7
SBMNH-VP-2019B.v2	*Balanus* sp.	Interlaminate figure	1	93	n.d.	1171	0.708357	0.000009	21.3
SBMNH-VP-2019C	*Balanus* sp.	Whole shell wall	1	98	n.d.	1340	0.708368	0.000010	21.2
SBMNH-VP-2019D	*Balanus* sp.	Whole shell wall	1	98	n.d.	1500	0.708435	0.000009	20.2
SBMNH-VP-2019D.v2	*Balanus* sp.	Interlaminate figure	1	76	n.d.	1061	0.708335	0.000009	21.7
SBMNH-VP-2019E	*Balanus* sp.	Whole shell wall	1	98	n.d.	1600	0.708402	0.000009	20.6
SBMNH-VP-2019F	*Balanus* sp.	Whole shell wall	1	98	n.d.	1566	0.708378	0.000009	21.0

Table 1. Strontium concentrations, $^{87}Sr/^{86}Sr$ compositions and apparent seawater strontium ages for shells and matrix leachates from deposits associated with sirenian fossils, Santa Rosa Island, California.—Continued

[n.d., not determined; µg/g, micrograms per gram; Ma, million years ago]

Sample identifier	Sample type	Subsample description	Stratigraphic horizon*	Percent leachable fraction#	Mole percent $MgCO_3$ in calcite†	Strontium concentration (µg/g)‡	$^{87}Sr/^{86}Sr$	±2 sigma	Apparent seawater-strontium age (Ma)@
SBMNH-VP-2031A	*Balanus* sp.	Whole shell wall	4	98	n.d.	1712	0.708411	0.000009	20.5
SBMNH-VP-2031A.v2	*Balanus* sp.	Interlaminate figure	4	90	n.d.	1808	0.708412	0.000010	20.5
SBMNH-VP-2031B	*Balanus* sp.	Whole shell wall	4	98	n.d.	1606	0.708418	0.000009	20.4
SBMNH-VP-2031B.v2	*Balanus* sp.	Interlaminate figure	4	98	n.d.	1797	0.708413	0.000010	20.5
SBMNH-VP-2031C	*Balanus* sp.	Whole shell wall	4	76	n.d.	1444	0.708365	0.000010	21.2
SBMNH-VP-2031C.v2	*Balanus* sp.	Interlaminate figure	4	95	n.d.	1202	0.708372	0.000009	21.1
SBMNH-VP-2031D	*Balanus* sp.	Whole shell wall	4	98	n.d.	1889	0.708378	0.000011	21.0
SBMNH-VP-2031E	*Balanus* sp.	Interlaminate figure	4	90	n.d.	1298	0.708379	0.000011	21.0
SBMNH-VP-2051-1	*Balanus* sp.	Whole shell wall	3	98	n.d.	1742	0.708433	0.000009	20.2
SBMNH-VP-2051-2a	*Balanus* sp.	Whole shell wall	3	98	n.d.	1399	0.708418	0.000010	20.4
SBMNH-VP-2051-2b	*Balanus* sp.	Whole shell wall	3	96	n.d.	2147	0.708421	0.000010	20.4
SBMNH-VP-2051-3	*Balanus* sp.	Whole shell wall	3	99	n.d.	1606	0.708416	0.000011	20.4
SBMNH-VP-2051M	*Balanus* sp.	Interlaminate figure	3	91	n.d.	2410	0.708426	0.000009	20.3
SBMNH-VP-2051O	*Balanus* sp.	Interlaminate figure	3	95	n.d.	1930	0.708427	0.000009	20.3
SRI-18009A-1B3 matrix	Matrix leach	Gray sand inside shell	2	37	n.d.	212	0.707963	0.000009	n.d.
SRI-18009A-3A4 matrix	Matrix leach	Brown sand outside shell	2	36	n.d.	230	0.707980	0.000009	n.d.
SBMNH-VP-2019A-m	Matrix leach	Tan sand inside barnacle	1	50	n.d.	44	0.708007	0.000009	n.d.
SBMNH-VP-2031A-m	Matrix leach	Tan sand inside barnacle	4	43	n.d.	841	0.708074	0.000010	n.d.
SBMNH-VP-2051-m1	Matrix leach	Gray sand inside barnacle	3	63	n.d.	906	0.708003	0.000015	n.d.
SBMNH-VP-2051-m2	Matrix leach	Gray–tan sand inside barnacle	3	38	n.d.	510	0.708030	0.000012	n.d.

*See figure 2 for stratigraphic relations: 1–extracted-sirenian conglomerate layer; 2–lower sandstone layer; 3–mudstone/siltstone layer; 4–original-sirenian sandstone layer.

#Determined by gravimetry before and after acetic acid treatment. Leachable component is assumed to be carbonate (calcite and aragonite). Uncertainties estimated to be less than ±5 percent at the 95-percent confidence level.

†Determined by X-ray diffraction. No aragonite peaks were observed. Uncertainties estimated to be less than ±2 mole-percent at the 95-percent confidence level.

‡Determined by isotope-dilution thermal-ionization mass spectrometry. Uncertainties are estimated to be less than ±1.0 percent at the 95-percent confidence level.

@Calculated from measured $^{87}Sr/^{86}Sr$ value using LOESS-6 seawater strontium age-calibration of McArthur and others (2020). Uncertainties for individual age values are not provided to avoid giving credibility to individual analysis affected by diagenetic alteration. See text for discussion of best age estimates.

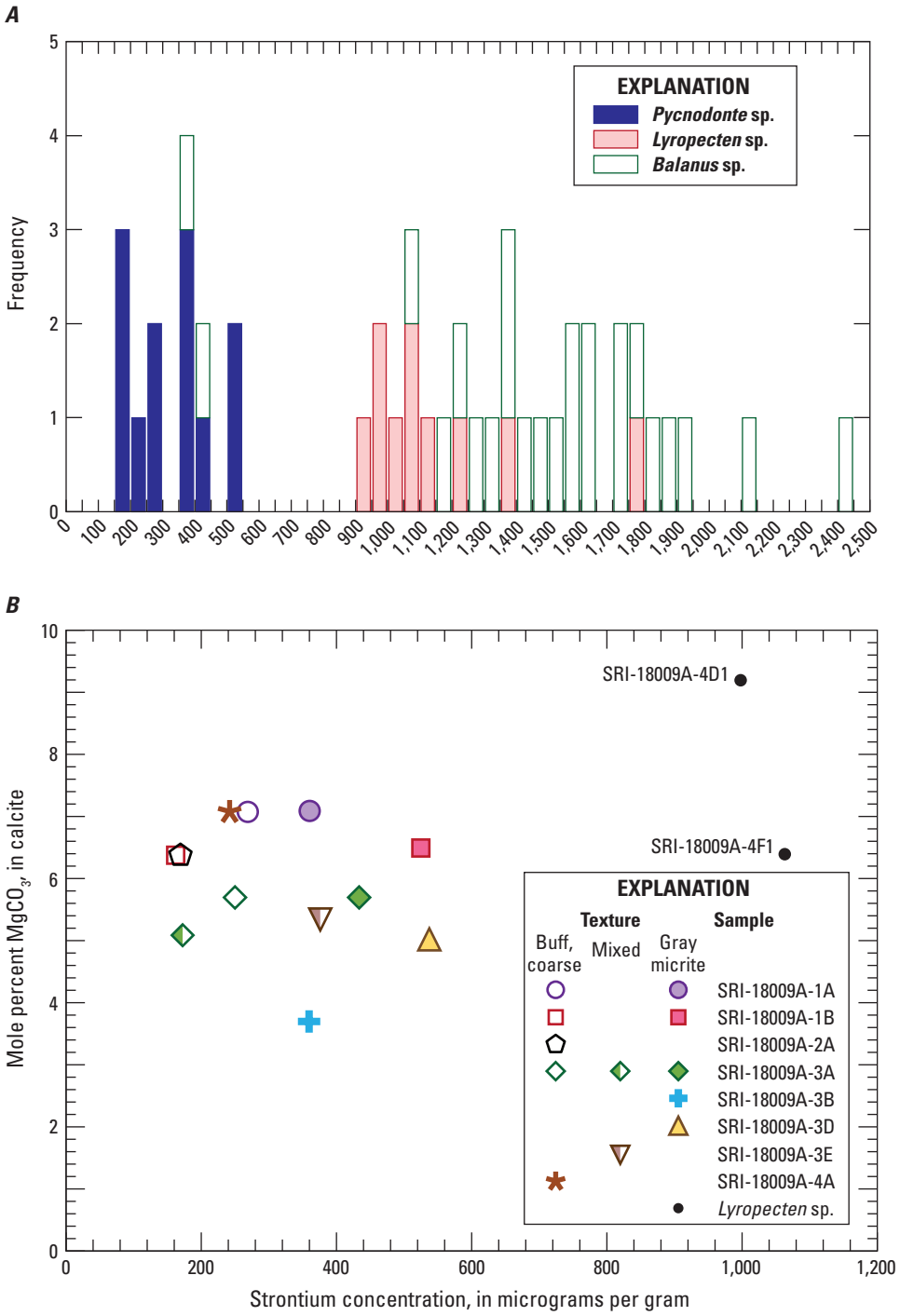

Figure 7. Bar graph showing frequency of strontium concentrations determined by isotope dilution for 46 analyses of shell samples distinguished by genus type in *A*, and bivariant scatterplot of strontium concentrations versus mole-percent magnesite ($MgCO_3$) in calcite ($CaCO_3$) determined by X-ray diffraction in *B*. In *B*, subsamples with strontium concentrations less than 600 micrograms per gram are from *Pycnodonte* sp. specimens with subsamples classified by shell texture and color. Data are from table 1.

Strontium Isotopic Compositions

Like strontium concentrations, $^{87}Sr/^{86}Sr$ values vary widely, and are broadly correlated to genus type (table 1). Subsamples of *Pycnodonte* specimens exhibit the greatest range of $^{87}Sr/^{86}Sr$ values (0.70791–0.70840), whereas much more restricted ranges are observed for subsamples of *Balanus* (0.70834–0.70844) and *Lyropecten* (0.70843–0.70845) specimens. Matrix leachates also show substantial $^{87}Sr/^{86}Sr$ variability, although all $^{87}Sr/^{86}Sr$ values are substantially lower (0.70796–0.70807) than most subsamples of shell carbonate.

$^{87}Sr/^{86}Sr$ values also show positive, nonlinear correlations with strontium concentrations, where subsamples with the highest strontium concentrations also have highest $^{87}Sr/^{86}Sr$ values (fig. 8). This is most evident for subsamples of *Pycnodonte* specimens that show a steeply sloping trend in $^{87}Sr/^{86}Sr$–strontium space. Results for subsamples of *Balanus* shell show a similar, but more subdued trend with substantial scatter. Subsamples of *Lyropecten* show the most restricted range of $^{87}Sr/^{86}Sr$ values over a large range of elevated strontium concentrations.

Closer examination of data for several thick *Pycnodonte* specimens indicate that different subsamples from the same shell can have very different analytical results (fig. 9) instead of the single, homogeneous $^{87}Sr/^{86}Sr$ composition expected for shells of a living marine mollusk. Subsamples of buff, coarsely crystalline material from three individual shells (SRI-18009A-1A, SRI-18009A-1B, and SRI-18009A-3A) have $^{87}Sr/^{86}Sr$ values and strontium concentrations that are substantially lower than values obtained from darker gray, finely laminated material from the same shells. This same pattern was observed for smaller shell fragments where only one textural type was subsampled. Lower concentrations imply a postmortem loss of strontium during diagenesis; however, strontium loss alone would not affect $^{87}Sr/^{86}Sr$ values. Therefore, the lower $^{87}Sr/^{86}Sr$ values in those same samples indicate that strontium from a different isotopic reservoir was introduced at the same time bulk strontium losses occurred.

In contrast, subsamples of multiple *Lyropecten* specimens have a highly restricted range of $^{87}Sr/^{86}Sr$ values that fall within the limits of analytical uncertainty despite a large variation in strontium concentrations, ranging from 924 to 1,755 µg/g (fig. 10). Unlike results from subsamples of *Pycnodonte* shells, two subsamples from a single *Lyropecten* shell (SBMNH-VP-2055 and SBMNH-VP-2055.v2) yielded $^{87}Sr/^{86}Sr$ values that are identical to the sixth decimal place (0.708444), even though the two subsamples show large differences in strontium concentration (1,755 and 1,138 µg/g). There is no statistically significant correlation between $^{87}Sr/^{86}Sr$ and strontium concentrations, as indicated by an extremely low slope (3×10^{-9}) and r^2 value (0.0247) for a simple linear regression. In addition, $^{87}Sr/^{86}Sr$ values for samples from three different sedimentary horizons in approximately 8 m of section show no tendencies to correlate with higher or lower stratigraphic position (fig. 10). Individual results for 10 analyses from 9 individual specimens or shell fragments yielded a mean $^{87}Sr/^{86}Sr$ value of 0.708440±0.000010 (±2SD).

Results for subsamples of barnacle (*Balanus* sp.) shells show compositional patterns intermediate between *Pycnodonte* and *Lyropecten* shells (fig. 8). $^{87}Sr/^{86}Sr$ values scatter beyond analytical uncertainty and show a crude correlation with strontium concentrations (fig. 11). The correlation is improved for phase 2 subsamples that more carefully targeted clean, dense, interlaminate figure. Those analyses show a better-defined curvilinear trend similar to that observed in *Pycnodonte* subsamples, where the two analyses with the highest strontium concentrations (SBMNH-VP-2051M and SBMNH-VP-2051O) also have the highest values of $^{87}Sr/^{86}Sr$. Those two results, plus two subsamples of whole shell wall (SBMNH-VP-2019D and SBMNH-VP-2051-1), approach but do not exceed the mean $^{87}Sr/^{86}Sr$ value obtained from *Lyropecten* samples (thick, gray horizontal line in fig. 11). Interestingly, two *Balanus* subsamples with the lowest strontium concentrations (SBMNH-VP-2019A and SBMNH-VP-2019B) do not have the lowest $^{87}Sr/^{86}Sr$ values and do not follow this trend.

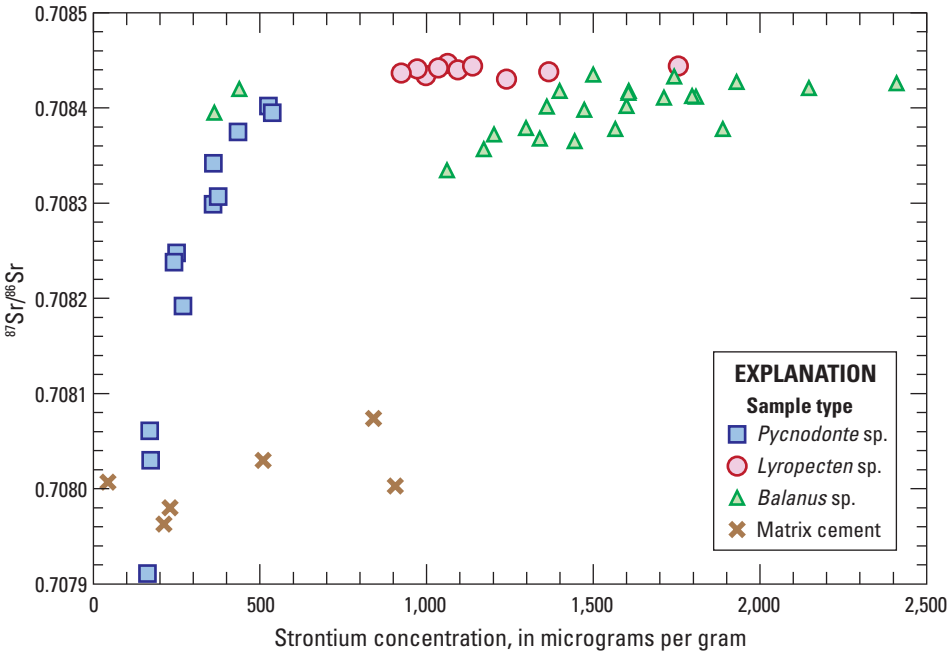

Figure 8. Graph showing bivariant plot of strontium concentrations versus strontium isotopic composition ($^{87}Sr/^{86}Sr$) for all specimens of shell material and acetic acid leachates of matrix calcite. Analytical error bars (2× standard deviation) are smaller than symbol size. Data are from table 1.

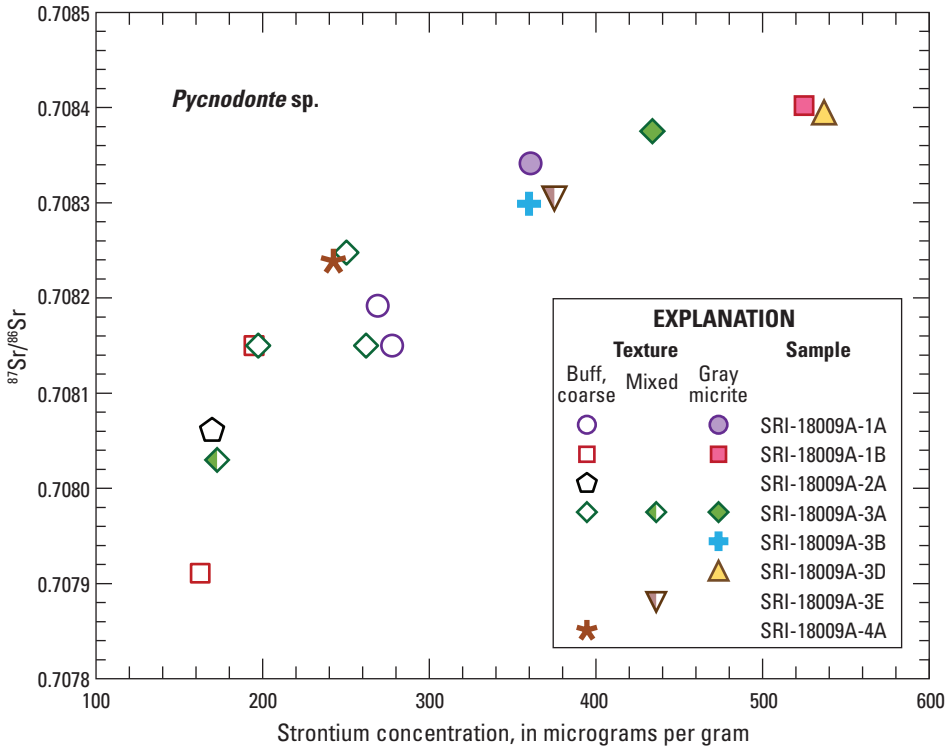

Figure 9. Graph showing bivariant plot of strontium concentrations versus strontium isotopic composition ($^{87}Sr/^{86}Sr$) for specimens of *Pycnodonte* sp. shell material. Subsamples from the same shell are shown using the same symbol that is either filled for dark-gray micritic material, open for buff, coarse-grained material, or partly filled for subsamples with mixed textures. Analytical error bars (2× standard deviation) are smaller than symbol size. Individual data are from table 1.

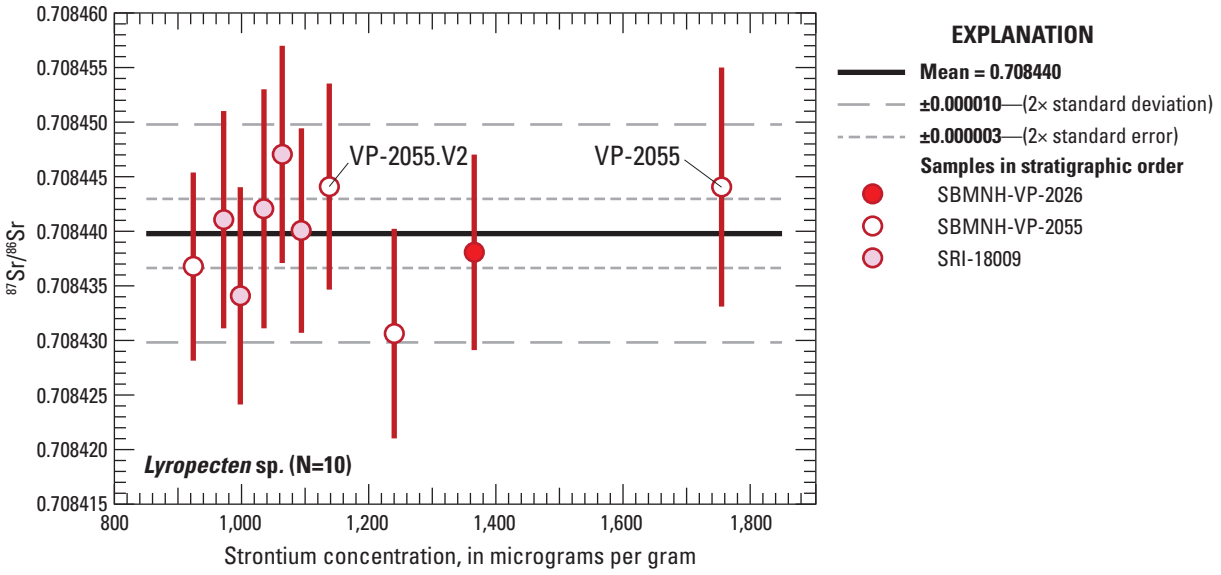

Figure 10. Graph showing bivariant plot of strontium concentrations versus strontium isotopic composition ($^{87}Sr/^{86}Sr$) for specimens of *Lyropecten* sp. shell material. Error bars for individual data points are shown as 2-sigma uncertainties. Subsamples from the same shell are labeled as VP-2055 and VP-2055.v2. Individual data are from table 1. Uncertainties for the mean $^{87}Sr/^{86}Sr$ value are given as both 2× standard deviation (2SD; long-dashed lines) and 2× standard error (2SE=2SD/sqrt(N); short-dashed lines).

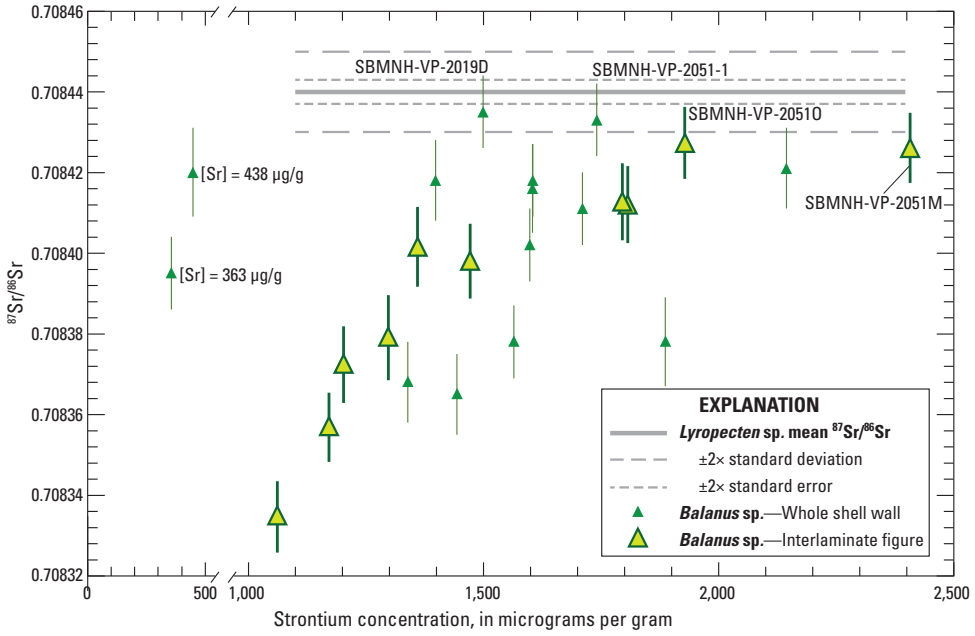

Figure 11. Graph showing bivariant plot of strontium concentrations versus strontium isotopic composition ($^{87}Sr/^{86}Sr$) for specimens of *Balanus* sp. shell material. Error bars for individual data points are given as 2-sigma uncertainties. Results for phase 1 subsamples consisting of whole shell walls are shown as small solid triangles. Results for phase 2 subsamples consisting of interlaminate figure (see fig. 6 for differences) are shown as large, filled triangles. Note the broken scale for the x-axis which allows plotting of two phase 1 subsamples with strontium concentrations less than 500 micrograms per gram (µg/g). Mean value and uncertainties determined for *Lyropecten* sp. subsamples are shown as horizontal gray lines for comparison (see fig. 10). Individual data are from table 1.

Strontium Chronostratigraphy

Use of $^{87}Sr/^{86}Sr$ data to estimate marine chronostratigraphic ages requires that the analyzed materials have retained their original strontium isotopic compositions inherited from seawater at the time of shell formation (McArthur and others, 2020). The large range in $^{87}Sr/^{86}Sr$ variation obtained for some of the shell material in this study indicates that not all samples meet that requirement. Shell material was not screened using secondary electron-microscope imaging or petrographic analyses as suggested elsewhere (Cochran and others, 2010; Knoll and others, 2016; Buczek and others, 2021). Furthermore, XRD results indicating the absence of aragonite and a lack of systematic variations of $MgCO_3$ contents in altered and unaltered *Pycnodonte* and *Lyropecten* samples did not provide useful information for sample screening. However, relations between $^{87}Sr/^{86}Sr$ and strontium concentrations provided a basis to discriminate between materials that have been compromised by secondary alteration from those that are more suitable for age assignment. Marcano and others (2015) advocated for the use of strontium concentration to determine the viability of $^{87}Sr/^{86}Sr$ preservation, and warned that other indicators of alteration, such as cathodoluminescence, manganese-iron concentration, and the presence of metastable mineral phases, such as aragonite and high-magnesium calcite, can be problematic.

Diagenetic Modification

Hyperbolic curves between $^{87}Sr/^{86}Sr$ and strontium concentration such as those observed in figures 8 and 9 can be modeled by simple mixing relations between two end-members (chap. 16 of Faure and Mensing, 2005). The shape of the mixing curve depends on the differences between both strontium concentrations and $^{87}Sr/^{86}Sr$ values in each end-member. Results for *Pycnodonte* subsamples most clearly reflect interactions between the unaltered shell material and diagenetic solutions involving an overall loss of the original strontium (unaltered shell end-member) and incorporation of secondary strontium with lower $^{87}Sr/^{86}Sr$ introduced during recrystallization (matrix cement end-member) (fig. 12*A*). The unaltered shell end-member is assumed to be best represented by the uniform $^{87}Sr/^{86}Sr$ and high strontium-concentration values obtained for *Lyropecten* specimens (fig. 10). Unlike this component, the diagenetic component is not well-defined by a cluster of points for either shells or matrix-cement samples. Despite the lack of a known diagenetic composition, results from *Pycnodonte* subsamples form a reasonably well-defined straight linear array of points on a plot of $^{87}Sr/^{86}Sr$ versus reciprocal strontium concentration (fig. 12*B*), which reflects the mathematical consequence of binary mixing (Faure and Mensing, 2005).

To estimate compositions of a potential low $^{87}Sr/^{86}Sr$ end-member, clastic sediment containing calcite cement and associated with *Pycnodonte* and *Balanus* fossils was analyzed by acetic acid leaching. The leaching method was intended to dissolve calcite without releasing strontium from silicate phases (including clays) containing $^{87}Sr/^{86}Sr$ signatures that are not diagnostic of a diagenetic fluid. Although all leachate samples had $^{87}Sr/^{86}Sr$ values lower than most shell samples, the two samples associated with *Pycnodonte* shells (SRI-18009A-1B3 matrix and SRI-18009A-3A4 matrix) showed the greatest consistency in terms of both strontium concentration (212 and 230 µg/g) and $^{87}Sr/^{86}Sr$ (0.707963 and 0.707980). Even though those two matrix calcite samples do not align perfectly with the low strontium end of the hyperbolic data array (fig. 12), the $^{87}Sr/^{86}Sr$ values of these samples are consistent with a postdepositional reservoir of strontium that was available to exchange with carbonate in *Pycnodonte* shells during diagenesis.

Mixing calculations between strontium in a hypothetical diagenetic component (approximated using the lowest $^{87}Sr/^{86}Sr$ value of 0.707963 obtained for sample SRI-18009A-1B3 matrix) and seawater strontium incorporated into the shells at the time of their formation (0.708440) closely approximates the range of values observed in *Pycnodonte* shell subsamples (fig. 12). Strontium concentrations in both end-members were adjusted so that the mixing line fits the observed linear array more closely (700 µg/g for the unaltered shell end-member and 150 µg/g for the matrix cement end-member). We note that the 700 µg/g value used for the unaltered shell end-member is within the range of values (albeit at the low end) reported for shells from modern oysters in Milliman (1974). In this mixing model, results suggests that even the *Pycnodonte* subsamples with the highest $^{87}Sr/^{86}Sr$ may contain as much as 30 percent of their strontium derived from the matrix cement component despite the apparent lack of alteration observed while sampling under binocular magnification.

Rather than simple mixing of two solids as modeled here, more complex processes of fluid-solid interaction, recrystallization, and strontium exchange likely explain the lower $^{87}Sr/^{86}Sr$ values in *Pycnodonte* subsamples. Pederson and others (2019) described conditions affecting diagenesis that range from fluid-dominated, which are systems open to active advection of pore fluids and aqueous dissolution and reprecipitation (Veizer, 1983), to rock-dominated, where systems are closed to fluid interactions and favor diffusion-driven transport of components between sediments and the enclosed shells. The presence of thin layers of organic materials in between calcium carbonate mineral layers further complicates digenetic behavior of shell material in both early and later phases of diagenesis (Jonas and others, 2017). Other authors have observed similar results for mollusk shells from the Pacific coast of North America, where diagenetically altered samples have lower $^{87}Sr/^{86}Sr$ values than those interpreted to have remained pristine (Gröcke and others, 2007; Buczek and others, 2021). Data for samples of matrix cement and shell aliquots in this study demonstrate that *Pycnodonte* shell material interacted with postdepositional fluids, and that shell material with lower $^{87}Sr/^{86}Sr$ values is caused by the addition of secondary cement or strontium exchange during recrystallization. Because of this alteration, strontium isotopic compositions of those subsamples yield erroneous chronostratigraphic ages.

Data for *Balanus* shells show diagenetic effects similar to those seen in *Pycnodonte* shells, although to smaller degrees (figs. 8 and 11). The relation between strontium and $^{87}Sr/^{86}Sr$ observed for subsamples of interlaminate figure indicates that

even the relatively nonporous portions of the shell walls can be affected by strontium exchange with diagenetic fluids having lower $^{87}Sr/^{86}Sr$. It is notable that none of the *Balanus* subsamples have $^{87}Sr/^{86}Sr$ values higher than the mean value observed in *Lyropecten* shells, although several individual *Balanus* $^{87}Sr/^{86}Sr$ analyses are within error overlap of that value (fig. 11).

Two *Balanus* samples do not show the same diagenetic trajectory observed in all *Pycnodonte* shells and the rest of the *Balanus* suite (fig. 8). The substantially lower strontium concentrations in SBMNH-VP-2019A (438 µg/g) and SBMNH-VP-2019B (363 µg/g) relative to other *Balanus* specimens (1,061–2,410 µg/g) suggest substantial strontium loss during diagenesis. Despite the lower strontium concentrations, the $^{87}Sr/^{86}Sr$ values for those two samples remain elevated. We posit that this pattern can be explained if the alteration of *Balanus* shells took place in two different burial environments, following a scenario suggested by McArthur and others (2020). For specimens with the lowest strontium concentrations, alteration leading to strontium loss likely took place in a shallow burial environment where pore fluids were dominated by seawater that was present shortly after sediments were deposited. Thus, alteration of shells would result in an overall strontium loss while any exchanges of strontium between solids and fluids would not be noticeable due to the similarity of $^{87}Sr/^{86}Sr$ values in the two geochemical reservoirs. However, with increased burial, pore fluids likely became isolated from seawater and started to acquire strontium from water/rock interactions with the clastic sediment. Values of $^{87}Sr/^{86}Sr$ in those sediments were mostly derived from isotopically juvenile continental-margin sources with values less than 0.707 (Kistler and Peterman, 1973, 1978; Kistler and others, 2003; Rosenbauer and others, 2013). Diagenetic alteration involving those kinds of fluids would result in not only strontium losses, but a noticeable $^{87}Sr/^{86}Sr$ shift towards lower values like those obtained here from sediment leachates. This scenario illustrates the inherent complexity that can occur during burial and alteration of marine sediment. It also introduces the possibility that some of the strontium-$^{87}Sr/^{86}Sr$ scatter observed in *Balanus* specimens (fig. 11) may have been caused by similarly complex burial and isotope-exchange histories.

Despite evidence of post-depositional modifications in *Pycnodonte* and *Balanus* shells, multiple samples of thin *Lyropecten* shell fragments have $^{87}Sr/^{86}Sr$ values that are identical within analytical error regardless of their range in strontium concentrations (924–1,755 µg/g) (fig. 10). The greater resistance to secondary alteration for some shells (for example, *Lyropecten*) versus others is likely related to differences in vital effects of biomineralization (metabolic and physiological processes), different organisms having different structural organization of shell materials, amount and type of organic content, original mineralogic stability, and local geochemical conditions in the diagenetic environment (Pérez-Huerta and Andrus, 2010; Pérez-Huerta and others, 2018). Effects observed in one sample suite may not dictate how those same materials behave in another, and diagenesis needs to be evaluated on a case-by-case basis (Ullmann and Korte, 2015). Nevertheless, the observed geochemical outcome for *Lyropecten* results represents the "ultimate test of good preservation," where values of $^{87}Sr/^{86}Sr$ are reproducible within a set of multiple shell samples from the same stratigraphic interval (McArthur and others, 2020, p. 220). Consequently, the mean $^{87}Sr/^{86}Sr$ value (and its 2× standard error precision) obtained for the 10 *Lyropecten* analyses (0.708440±0.000003) is interpreted as the best estimate for unaltered seawater strontium isotope composition at the time the sirenians were alive.

Age Estimates Based on Seawater Strontium Evolution

Strontium isotopic compositions of minerals precipitated from seawater can be used to estimate ages of those materials based on the well-calibrated $^{87}Sr/^{86}Sr$ evolution of seawater. Changes in seawater strontium compositions are largely a balance between input functions attributed to hydrothermal alteration of mid-ocean-ridge basalts and weathering of continental crust with associated riverine fluxes (Peucker-Ehrenbrink and Fiske, 2019). Those global processes have differed in intensity over different periods of Earth history, causing shifts towards more radiogenic values (higher $^{87}Sr/^{86}Sr$) when rates of continental weathering were greater, or less radiogenic values (lower $^{87}Sr/^{86}Sr$) when rates of oceanic volcanism were greater. The concept of evolving seawater strontium compositions has been known for more than 50 years (Peterman and others, 1970), with an ever-increasing understanding of time-dependent $^{87}Sr/^{86}Sr$ variations as more materials of known age have been analyzed (Elderfield, 1986; Veizer and others, 1997; McArthur, 1994; McArthur and others, 2001, 2006, 2012, 2020).

Chronostratigraphic age estimates were calculated for strontium isotope data listed in table 1 using values in the LOESS-6 look-up table published by McArthur and others (2020) that are based on statistical regressions of worldwide marine strontium data. The seawater strontium isotope evolution curve is unambiguous for Cenozoic marine deposits compared to other age intervals (inset in fig. 13*A*), increasing monotonically, albeit nonlinearly, from about 40 Ma to the present. The slope of the evolution curve between about 30 and 15 Ma is particularly well-established because the high rate of change over this period provides exceptional precision for calculated dates (McArthur and others, 2020).

Apparent ages were calculated for the shell data using individual, measured $^{87}Sr/^{86}Sr$ values to interpolate ages between the closest age-composition intervals given for 0.05 Ma intervals in the LOESS-6 lookup table. Resulting values range from 31.9 to 20.0 Ma (fig. 13*A*; table 1), despite the fact that all specimens were collected from a narrow (approximately 13-m-thick) stratigraphic interval. Older apparent ages are interpreted to be a consequence of the lower $^{87}Sr/^{86}Sr$ values caused by postdepositional interaction between shells and diagenetic fluids as described above. Sources of strontium with $^{87}Sr/^{86}Sr$ values lower than seawater include the clastic host sediment generated from rocks in a continental margin setting, and Miocene basaltic volcanic and intrusive rocks (units Tv and Ti, respectively) that are closely associated with the marine

sediments on Santa Rosa Island (fig. 1*B*). As such, apparent ages calculated for those altered subsamples are erroneous, and uncertainties for individual age values are not estimated in table 1 to avoid giving credibility to any individual analysis.

However, results for all 10 analyses of *Lyropecten* shells yield a narrow range of $^{87}Sr/^{86}Sr$ values that are interpreted to represent unaltered values of $^{87}Sr/^{86}Sr$ incorporated from seawater at the time of shell formation. Values of $^{87}Sr/^{86}Sr$ for individual analyses of the *Lyropecten* shells are within analytical error and yield a sample population that is statistically indistinguishable from a normal distribution about a mean value of 0.7084397. An estimate of uncertainty for the mean follows equation 7.2 in McArthur and others (2020), where the 95-percent confidence interval (CI) is equal to $\pm t \times SE$, where t is the Student-t multiplier for a two-sided normal distribution with 9 degrees of freedom, and SE is the standard error for the 10 analyses, or $CI = \pm 2.262 \times 0.00000159 = \pm 0.0000036$. The $^{87}Sr/^{86}Sr$ mean value for *Lyropecten* shells was rounded to a value of 0.708440±0.000004. Calculation of a LOESS-6 chronostratigraphic age for that $^{87}Sr/^{86}Sr$ mean and 95-percent CI value results in a numerical age and uncertainty of 20.08±0.11 Ma (fig. 13*B*). There are no systematic differences of $^{87}Sr/^{86}Sr$ results from *Lyropecten* samples collected from different strata hosting samples SRI-18009, SBMNH-VP-2055, and SBMNH-VP-2026 (figs. 2 and 10). As such, we cannot resolve age differences over the approximately 8 m of intervening sediment, implying that deposition rates were faster than approximately 0.04 millimeters per year. Based on strontium isotope results from *Lyropecten* sp. shell fragments, we conclude that the two sirenian fossils discovered on Santa Rosa Island have statistically indistinguishable ages of 20.08±0.11 Ma.

This date provides a precise datum that shows sirenian expansion into the northeastern Pacific region had occurred by the beginning of the early Miocene. A previously reported, potentially older dugongid specimen is represented by a partial skull with mandible from a hard beach cobble that was attributed to nearby exposures of the Nye Mudstone along the central Oregon coast (Domning and Ray, 1986). Because the fossil was found as float, its stratigraphic position within the upper Oligocene to lower Miocene (25–18 Ma) Nye Mudstone strata cannot be determined with precision. Thus, the precise age of the Oregon specimen remains questionable. In contrast, the skull and partially intact skeleton extracted from Santa Rosa Island and precisely dated here will allow for a more complete taxonomic assessment of this fossil sirenian, and contribute critical information on the nature of early sirenians and their dispersal in this part of the northeastern Pacific region.

Chronostratigraphic Implications of Fossil-Bearing Strata

The age of fossil invertebrate shells from the sirenian fossil-bearing stratigraphic section constrains the timing of deposition of the associated marine transitional lithofacies. Although the approximately 13-m-thick section sampled in this study is only a small portion of the full local late Oligocene and early Miocene stratigraphic section, results imply that a change from near-shore, sand-dominated sedimentation (Vaqueros Sandstone) to deeper water, silt and clay sedimentation (Rincon formation) was well underway by 20 Ma on what is now Santa Rosa Island. Based on herbivorous feeding habits of sirenians, the presence of sirenian fossils implies a shallow-water, coastal environment (Domning, 1978, Aranda-Manteca and others, 1994; Domning, 2018), as does the presence of neritic barnacles and oysters in the same host deposits. This evidence, along with the fact that both sirenian specimens were found mostly articulated, implies that postmortem transport of the sirenian carcasses to deeper water was unlikely. We conclude that the observed lithostratigraphy is consistent with a progressive marine transgression that lacked erosional unconformities or depositional hiatuses, and shows only changes in grain size of the sediment supplied to increasingly lower energy environments.

The timing determined for this stratigraphic interval agrees broadly with late Oligocene to early Miocene ages determined for the Vaqueros Sandstone, and more closely with early Miocene ages for the Rincon formation, based on age determinations for these units on the coastal mainland. However, the inferred depositional environment for the sirenian site at 20 Ma is shallow coastal water. Strict temporal correlation to formational characteristics observed on the mainland may not be possible for deposits on Santa Rosa Island if facies changes were substantial over the intervening distance (currently >50 kilometers [km] across the Santa Barbara Channel), if late Cenozoic tectonic transrotation (both tectonic translation and rotation) of the island crustal block relative to the mainland was significant (for example, Atwater, 1998), or both. Thus, based on either age or lithostratigraphy, definitive assignment of the fossil-bearing strata to one formation or the other is equivocal and essentially arbitrary. The 20.08 Ma strontium chronostratigraphic age determined for the fossil-bearing strata is within, but at the very youngest end of the 25 to 20 Ma range initially ascribed to the Santa Rosa Island sirenian fossils (National Park Service, 2018).

Accurate paleobiogeographic reconstruction of early sirenian dispersal also must consider changes in paleogeography that occurred over the timespan since deposition. Starting at about 18 Ma, crustal blocks along the southern California coast, including blocks composed of what is now the modern northern Channel Islands, were subjected to tectonic rotation and translation towards the northwest (Atwater, 1998). Therefore, the original paleolatitude (north-south component of transport) of the sirenian-bearing strata was as much as 200 km south of its current position. Since burial, the total displacement of the Santa Rosa fossil sirenians by tectonic transrotation along a northwesterly trajectory away from the paleoequator is more than 300 km from their original depositional location to the southeast, near modern San Diego.

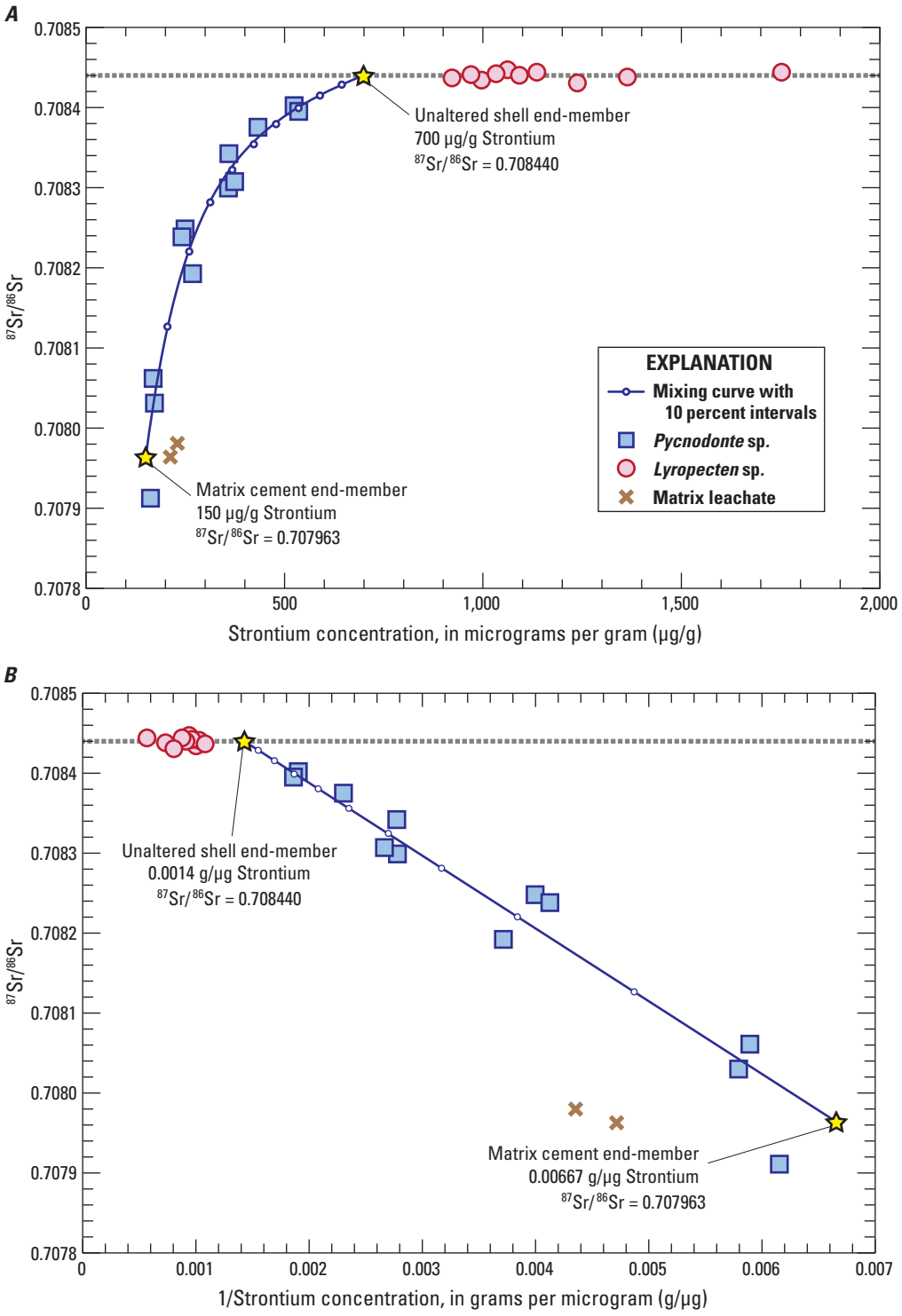

Figure 12. Graphs showing relations between $^{87}Sr/^{86}Sr$ ratios and strontium concentrations in *A* and reciprocal strontium concentration in *B* for subsamples of mollusk shells. Also shown are results for acetic acid leachates of two sandstone subsamples (brown crosses) and simple binary mixing curves calculated for end-members with $^{87}Sr/^{86}Sr$ compositions defined by the average of *Lyropecten* shells (dotted gray line, assumed to represent the strontium composition of seawater at the time of deposition), and post-depositional calcite cement with a $^{87}Sr/^{86}Sr$ composition defined by the acetic acid leachate of subsample SRI-18009A-1B3 matrix. Strontium concentrations of mixing end-members were adjusted to best match the linear array shown in *B*. Small, open circles on the mixing lines represent 10 percent mixing intervals. µg/g, micrograms per gram; g/µg, grams per microgram.

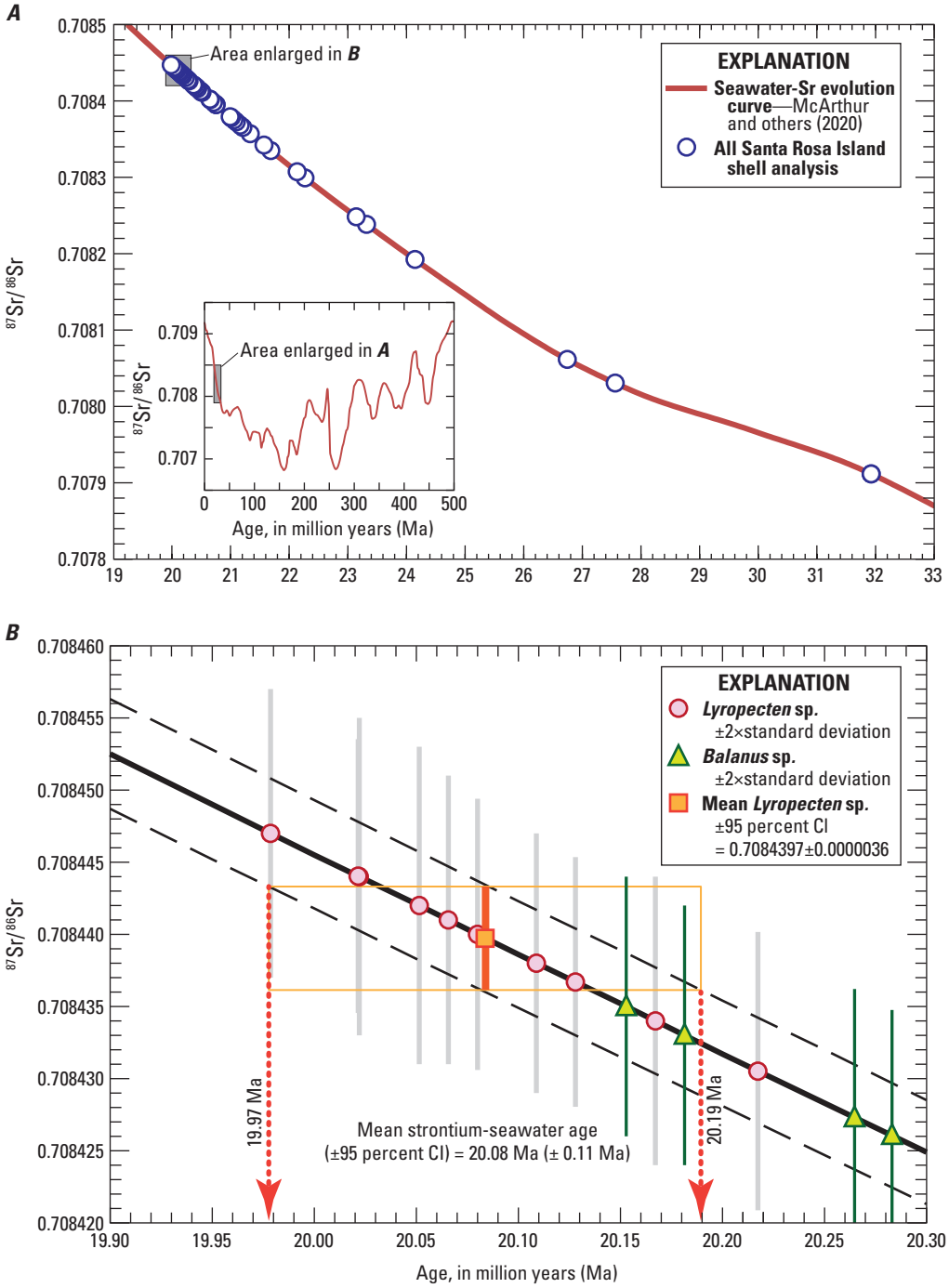

Figure 13. Graphs of variation of marine $^{87}Sr/^{86}Sr$ through time, showing results for Santa Rosa Island sirenian site invertebrate shells. *A* shows a portion of the LOESS-6 statistical fit to worldwide fossil data that defines the seawater strontium (Sr) evolution curve of McArthur and others (2020), with $^{87}Sr/^{86}Sr$ compositions for all shell analyses from the Santa Rosa Island sirenian site plotted on the main curve. Inset shows strontium isotope compositions for the entire Phanerozoic. *B* shows the same curve and data as in *A*, but focusing on results having the least altered $^{87}Sr/^{86}Sr$ values (notably analyses of *Lyropecten* sp. shells). Uncertainties for individual analyses are shown as 2×standard deviation (2SD) error bars. Dashed black lines represent the uncertainty given for the LOESS fit. Mean $^{87}Sr/^{86}Sr$ value (orange square) and 95-percent confidence interval (CI) values (thick orange error bars and associated thin orange error box) calculated for 10 analyses of *Lyropecten* sp. shells define the mean seawater strontium age and associated uncertainties.

Conclusions

Recently discovered sirenian fossils on Santa Rosa Island in the Channel Islands National Park provide an opportunity to better understand the dispersal patterns of these aquatic mammals from the Caribbean into the Pacific Ocean. We report the results of strontium isotope chronostratigraphy for fossil bivalve shells and barnacle plates collected from the same sedimentary rocks where the sirenian specimens were found. Analyses of strontium concentrations and $^{87}Sr/^{86}Sr$ isotopes from well-preserved *Lyropecten* sp. shells provide an age estimate of 20.08±0.11 Ma for sedimentary strata spanning about 8.5 meters of section, with no systematic geochemical age differences between stratigraphically younger or older samples. In contrast, subsamples of other shell types (*Pycnodonte* sp. and *Balanus* sp.) from the same strata exhibit large variations in $^{87}Sr/^{86}Sr$ that generally correlate with strontium concentrations. In combination, strontium concentrations and $^{87}Sr/^{86}Sr$ provided a highly effective means of identifying materials that were subject to postdepositional alteration of original $^{87}Sr/^{86}Sr$ compositions. *Pycnodonte* shells are particularly susceptible to diagenesis; subsample compositions can be modeled as a binary mixing curve between an unmodified shell end-member and a diagenetic component containing less radiogenic $^{87}Sr/^{86}Sr$. Older seawater strontium age-estimates calculated from altered materials are clearly erroneous. Nevertheless, analyses of altered materials provided a means to definitively reject all but the specimens with the highest, most consistent $^{87}Sr/^{86}Sr$ values that yielded the youngest, most precise, and accurate chronostratigraphic age. Other strontium-based chronostratigraphic studies that show a range of $^{87}Sr/^{86}Sr$ values (and hence ages) for shells collected from a single stratigraphic horizon may be similarly affected by diagenetic effects. Definition of similar strontium $^{87}Sr/^{86}Sr$ trajectories towards a diagenetic component in these kinds of studies could help refine the isotopic composition of unaltered shell material to provide more accurate age estimates. Strontium chronostratigraphic results from this study confirm an early Miocene presence of sirenians in the northeastern Pacific region. The date determined here provides one of the most precise points for a temporal framework to use for further taxonomic studies of early sirenians and timing of their dispersal into the Pacific Ocean.

References Cited

Alroy, J., 2000, New methods for quantifying macroevolutionary patterns and processes: Paleobiology, v. 26, no. 4, p. 707–733, accessed December 29, 2022, at https://doi.org/10.1666/0094-8373(2000)026<0707:NMFQMP>2.0.CO;2.

Aranda-Manteca, F.J., Domning, D.P., and Barnes, L.G., 1994, A new middle Miocene sirenian of the genus *Metaxytherium* from Baja California and California—Relationships and palaeobiogeographic implications, *in* Berta, A., and Deméré, T.A., eds., Contributions in Marine Mammal Paleontology Honoring Frank C. Whitmore, Jr., Proceedings of the San Diego Society of Natural History, v. 29, p. 191–204.

Atwater, T.M., 1998, Plate tectonic history of southern California with emphasis on the western Transverse Ranges and northern Channel Islands, *in* Weigand, P.W., ed., Contributions to the geology of the Northern Channel Islands, southern California: Bakersfield, California, American Association of Petroleum Geologists Pacific Section Annual Meeting, MP-45, p. 1–8, accessed December 16, 2021, at https://doi.org/10.32375/1998-MP45.1.

Bonilla-Rodríguez, A.J., González, L.A., Walker, J.D., and Santos, H., 2014, Strontium isotope ($^{87}Sr/^{86}Sr$) stratigraphy from the *Coalcomana-Caprinuloidea* rudist assemblage in the Greater Antilles (Puerto Rico, Dominican Republic and Jamaica): Cretaceous Research, v. 50, p. 97–109, accessed October 5, 2021, at https://doi.org/10.1016/j.cretres.2014.04.008.

Buczek, A.J., Hendy, A.J.W., Hopkins, M.J., and Sessa, J.A., 2021, On the reconciliation of biostratigraphy and strontium isotope stratigraphy of three southern Californian Plio-Pleistocene formations: Geological Society of America Bulletin, v. 133, no. 1–2, p. 100–114, accessed October 5, 2021, at https://doi.org/10.1130/B35488.1.

Chave, K.E., 1952, A solid solution between calcite and dolomite: The Journal of Geology, v. 60, no. 2, p. 190–192, accessed October 18, 2021, at https://doi.org/10.1086/625949.

Checa, A.G., González-Segura, A., Rodríguez-Navarro, A.B., and Lagos, N.A., 2020, Microstructure and crystallography of the wall plates of the giant barnacle *Austromegabalanus psittacus*—A material organized by crystal growth: Journal of the Royal Society, Interface, v. 17, no. 164, p. 20190743, accessed October 5, 2021, at https://doi.org/10.1098/rsif.2019.0743.

Coates, A.G., Collins, L.S., Aubry, M.-P., and Berggren, W.A., 2004, The geology of the Darien, Panama, and the late Miocene-Pliocene collision of the Panama arc with northwestern South America: Geological Society of America Bulletin, v. 116, no. 11–12, p. 1327–1344, accessed March 7, 2022, at https://doi.org/10.1130/B25275.1.

Cochran, J.K., Kallenberg, K., Landman, N.H., Harries, P.J., Weinreb, D., Turekian, K.K., Beck, A., and Cobban, W.A., 2010, Effect of diagenesis on the Sr, O, and C isotope composition of late Cretaceous mollusks from the Western Interior Seaway of North America: American Journal of Science, v. 310, no. 2, p. 69–88, accessed October 19, 2021, at https://doi.org/10.2475/02.2010.01.

De Muynck, D., Huelga-Suarez, G., Van Heghe, L., Degryse, P., and Vanhaecke, F., 2009, Systematic evaluation of a strontium-specific extraction chromatographic resin for obtaining a purified Sr fraction with quantitative recovery from complex and Ca-rich matrices: Journal of Analytical Atomic Spectrometry, v. 24, no. 11, p. 1498–1510. [also available at https://doi.org/10.1039/b908645e.]

Dibblee, T.W., Jr., 1982, Geology of the Santa Ynez-Topatopa Mountains, Southern California, *in* Fife, D.L., and Minch, J.A., eds., Geology and mineral wealth of the California Transverse Ranges: Santa Ana, California, South Coast Geological Society Annual Symposium and Guidebook no. 10, Santa Ana, California, p. 41–56.

Dibblee, T.W., Jr., 1986, Geologic map of the Santa Barbara quadrangle, Santa Barbara County, California: Santa Barbara, Dibblee Geological Foundation Map DF-06, scale 1:24,000.

Dibblee, T.W., Jr., and Ehrenspeck, H.E., 1998, General geology of Santa Rosa Island, *in* Weigand, P.W., ed., Contributions to the geology of the Northern Channel Islands, southern California: Bakersfield, California, American Association of Petroleum Geologists Pacific Section Annual Meeting MP-45, p. 49–75. [also available at https://doi.org/10.32375/1998-MP45.4.]

Dibblee, T.W., Jr., Woolley, J.J., and Ehrenspeck, H.E., 1998, Geologic map of Santa Rosa Island, California: Dibblee Geological Foundation, Santa Barbara, California, Map DF-68, scale 1:24,000. [also available at https://ngmdb.usgs.gov/Prodesc/proddesc_71695.htm.]

Domning, D.P., 1978, Sirenian evolution in the North Pacific Ocean: Los Angeles, University of California Press, University of California Publications in Geological Sciences, v. 118, 146 p., with 1 appendix and 18 plates.

Domning, D.P., 2018, Sirenian evolution, *in* Würsig, B., Thewissen, J.G.M., and Kovacs, K.M., eds., Encyclopedia of Marine Mammals third edition: London, Academic Press, p. 856–859, accessed January 19, 2022, at https://doi.org/10.1016/B978-0-12-804327-1.00229-6.

Domning, D.P., and Ray, C.E., 1986, The earliest sirenian (Mammalia—Dugongidae) from the eastern Pacific Ocean: Marine Mammal Science, v. 2, no. 4, p. 263–276, accessed March 10, 2022, at https://doi.org/10.1111/j.1748-7692.1986.tb00135.x.

Elderfield, H., 1986, Strontium isotope stratigraphy: Palaeogeography, Palaeoclimatology, Palaeoecology, v. 57, no. 1, p. 71–90. [also available at https://doi.org/10.1016/0031-0182(86)90007-6.]

Faure, G., and Mensing, T.M., 2005, Isotopes – Principles and applications (3rd ed.): New York, John Wiley & Sons, 897 p.

Goldsmith, J.R., Graf, D.L., and Joensuu, O.I., 1955, The occurrence of magnesian calcites in nature: Geochimica et Cosmochimica Acta, v. 7, no. 5–6, p. 212–230, accessed October 18, 2021, at https://doi.org/10.1016/0016-7037(55)90033-8.

Gröcke, D.R., Hesselbo, S.P., and Findlay, D.J., 2007, Atypical diagenetic effects on strontium-isotope composition of Early Jurassic belemnites, Queen Charlotte Islands, British Columbia, Canada: Canadian Journal of Earth Sciences, v. 44, no. 2, p. 181–197, accessed October 5, 2021, at https://doi.org/10.1139/e06-087.

Jonas, L., Müller, T., Dahmen, R., Immenhauser, A., and Putlitz, B., 2017, Hydrothermal replacement of biogenic and abiogenic aragonite by Mg-carbonates-relation between textural control on effective element fluxes and resulting carbonate phase: Geochimica et Cosmochimica Acta, v. 196, p. 289–306. [also available at https://doi.org/10.1016/j.gca.2016.09.034.]

Keller, M.A., Tennyson, M.E., and Denison, R.E., 1996, Strontium isotope evidence for the age of the Vaqueros Formation and latest Oligocene marine transgression in the northern Santa Maria Province, Central California, chap. P *of* Keller, M.A., ed., Evolution of sedimentary basins/onshore oil and gas investigations—Santa Maria Province: U.S. Geological Survey Bulletin 1995–P,Q, p. P1–P8, accessed October 19, 2021, at https://doi.org/10.3133/b1995PQ.

Kistler, R.W., and Peterman, Z.E., 1973, Variations in Sr, Rb, K, Na, and initial $^{87}Sr/^{86}Sr$ in Mesozoic granitic rocks and intruded wall rocks in central California: Geological Society of America Bulletin, v. 84, no. 11, p. 3489–3512. [also available at https://doi.org/10.1130/0016-7606(1973)84<3489:VISRKN>2.0.CO;2.]

Kistler, R.W., and Peterman, Z.E., 1978, Reconstruction of crustal blocks of California on the basis of initial strontium isotopic compositions of Mesozoic granitic rocks: U.S. Geological Survey Professional Paper 1071, 17 p. [also available at https://doi.org/10.3133/pp1071.]

Kistler, R.W., Wooden, J.L., and Morton, D.M., 2003, Isotopes and ages in the northern Peninsular Ranges batholith, southern California: U.S. Geological Survey Open-File Report 03–489, 45 p. [also available at https://doi.org/10.3133/ofr03489.]

Kleinpell, R.M., 1938, Miocene stratigraphy of California: Tulsa, Oklahoma, American Association of Petroleum Geologists, and London, Thomas Murby and Co., 450 p., 22 plates.

Kleinpell, R.M., 1980, The Miocene stratigraphy of California revisited—AAPG Studies in Geology no. 11: Tulsa, Oklahoma, American Association of Petroleum Geologists, 349 p.

Knoll, K., Landman, N.H., Cochran, J.K., MacLeod, K.G., and Sessa, J.A., 2016, Microstructural preservation and the effects of diagenesis on the carbon and oxygen isotope composition of Late Cretaceous aragonitic mollusks from the Gulf Coastal Plain and the Western Interior Seaway: American Journal of Science, v. 316, no. 7, p. 591–613. [also available at https://doi.org/10.2475/07.2016.01.]

Long, X., Ma, Y., and Qi, L., 2014, Biogenic and synthetic high magnesium calcite—A review: Journal of Structural Biology, v. 185, no. 1, p. 1–14, accessed September 6, 2021, at https://doi.org/10.1016/j.jsb.2013.11.004.

Ludwig, K.R., Halley, R.B., Simmons, K.R., and Peterman, Z.E., 1988, Strontium-isotope stratigraphy of Enewetak Atoll: Geology, v. 16, no. 2, p. 173–177. [also available at https://doi.org/10.1130/0091-7613(1988)016<0173:SISOEA>2.3.CO;2.]

Marcano, M.C., Frank, T.D., Mukasa, S.B., Lohmann, K.C., and Taviani, M., 2015, Diagenetic incorporation of Sr into aragonitic bivalve shells—Implications for chronostratigraphic and palaeoenvironmental interpretations: The Depositional Record: a Journal of Biological, Physical and Geochemical Sedimentary Processes, v. 1, no. 1, p. 38–52, accessed October 15, 2021, at https://doi.org/10.1002/dep2.3.

McArthur, J.M., 1994, Recent trends in strontium isotope stratigraphy: Terra Nova, v. 6, no. 4, p. 331–358. [also available at https://doi.org/10.1111/j.1365-3121.1994.tb00507.x.]

McArthur, J.M., Howarth, R.J., and Bailey, R.R., 2001, Strontium isotope stratigraphy—LOWESS version 3; best fit to the marine Sr-isotope curve for 0–509 Ma and accompanying look-up table for deriving numerical age: The Journal of Geology, v. 109, no. 2, p. 155–170. [also available at https://doi.org/10.1086/319243.]

McArthur, J.M., Howarth, R.J., and Shields, G.A., 2012, Strontium isotope stratigraphy, *in* Gradstein, F.M., Ogg, J.G., Schmitz, M., and Ogg, G., eds., The Geologic Timescale 2012: Amsterdam, The Netherlands, Elsevier B.V., p. 127–144. [also available at https://doi.org/10.1016/B978-0-444-59425-9.00007-X.]

McArthur, J.M., Howarth, R.J., Shields, G.A., and Zhou, Y., 2020, Strontium isotope stratigraphy, chap. 7 *of* Gradstein, F.M., Ogg, J.G., Schmitz, M., and Ogg, G., eds., The Geologic Timescale 2020: Amsterdam, The Netherlands, Elsevier, p. 211–238. [also available at https://doi.org/10.1016/B978-0-12-824360-2.00007-3.]

McArthur, J.M., Rio, D., Massari, F., Castradori, D., Bailey, T.R., Thirlwall, M., and Houghton, S., 2006, A revised Pliocene record for marine-$^{87}Sr/^{86}Sr$ used to date an interglacial event recorded in the Cockburn Island Formation, Antarctic Peninsula: Palaeogeography, Palaeoclimatology, Palaeoecology, v. 242, no. 1–2, p. 126–136. [also available at https://doi.org/10.1016/j.palaeo.2006.06.004.]

Milliman, J.D., 1974, Marine carbonates. Recent sedimentary carbonates part 1: Berlin, Heidelberg, New York, Springer-Verlag, 375 p.

Minor, S.A., Bedford, D., Schmidt, K.M., Schumann, R.R., and Muhs, D.R., 2012, The ups and downs of the Santa Rosa Island Fault, Northern Channel Islands, California—More than simple strike slip [abs]: American Geophysical Union, Fall Meeting Abstracts, T33A-2647.

Minor, S.A., Kellogg, K.S., Stanley, R.G., Gurrola, L.D., Keller, E.A., and Brandt, T.R., 2009, Geologic map of the Santa Barbara coastal plain area, Santa Barbara County, California: U.S. Geological Survey Scientific Investigations Map 3001, scale 1:25,000, 1 sheet, pamphlet, 38 p., accessed October 19, 2021, at https://pubs.usgs.gov/sim/3001/.

Montes, C., Cardona, A., Jaramillo, C., Pardo, A., Silva, J.-C., Valencia, V., Ayala, C., Pérez-Angel, L.C., Rodriguez-Parra, L.A., Ramirez, V., and Nino, H., 2015, Middle Miocene closure of the Central American Seaway: Science, v. 348, no. 6231, p. 226–229, accessed October 22, 2021, at https://doi.org/10.1126/science.aaa2815.

Moore, D.M., and Reynolds, R.C., 1989, X-ray diffraction and the identification and analysis of clay minerals: Oxford, Oxford University Press, 378 p.

Muhs, D.R., Groves, L.T., Simmons, K.R., Schumann, R.R., and Minor, S.A., 2023, A complex record of last interglacial sea-level history and paleozoogeography, Santa Rosa Island, Channel Islands National Park, California, USA: Palaeogeography, Palaeoclimatology, Palaeoecology, v. 610, p. 111328, accessed January 6, 2023, at https://doi.org/10.1016/j.palaeo.2022.111328.

Muhs, D.R., Schumann, R.R., Groves, L.T., Simmons, K.R., and Florian, C.R., 2021, The marine terraces of Santa Cruz Island, California—Implications for glacial isostatic adjustment models of last-interglacial sea-level history: Geomorphology, v. 389, p. 107826, accessed October 22, 2021, at https://doi.org/10.1016/j.geomorph.2021.107826.

National Park Service, 2018, Mountaintop sea cows?: National Park Service web page, accessed March 7, 2022, at https://www.nps.gov/articles/mountaintop-sea-cows.htm.

Paces, J.B., 2022, Sr concentrations and $^{87}Sr/^{86}Sr$ data used to determine the Sr-chronostratigraphic age of sirenian fossils on Santa Rosa Island, Channel Islands National Park: California, USA: U.S. Geological Survey data release, https://doi.org/10.5066/P9GG6NB5.

Paces, J.B., Palmer, M.V., Palmer, A.N., Long, A.J., and Emmons, M.P., 2020, 300,000 yr history of water-table fluctuations at Wind Cave, South Dakota, USA—Scale, timing, and groundwater mixing in the Madison Aquifer: Geological Society of America Bulletin, v. 132, no. 7-8, p. 1447–1468. [also available at https://doi.org/10.1130/B35312.1.]

Pederson, C., Mavromatis, V., Dietzel, M., Rollion-Bard, C., Nehrke, G., Neuser, R., Jöns, N., Jochum, K.P., and Immenhausera, A., 2019, Diagenesis of mollusc aragonite and the role of fluid reservoirs: Earth and Planetary Science Letters, v. 514, p. 130–142, accessed March 9, 2022, at https://doi.org/10.1016/j.epsl.2019.02.038.

Pérez-Huerta, A., and Andrus, C.F.T., 2010, Vital effects in the context of biomineralization, *in* Fernández Díaz, L., and Astilleros García-Monge, J.M., eds., Biominerals and Biomineralization Processes: Seminarios de la Sociedad Española de Mineralogía. Sociedad Española de Mineralogía, Madrid, v. 7, p. 35–45, accessed March 8, 2022, at https://www.semineral.es/websem/PdfServlet?mod=archivos&subMod=publicaciones&archivo=SEMINARIO_SEM_7_035.pdf.

Pérez-Huerta, A., Coronado, I., and Hegna, T.A., 2018, Understanding biomineralization in the fossil record: Earth-Science Reviews, v. 179, p. 95–122, accessed March 8, 2022, at https://doi.org/10.1016/j.earscirev.2018.02.015.

Peterman, Z.E., Hedge, C.E., and Tourtelot, H.A., 1970, Isotopic composition of strontium in sea water throughout Phanerozoic time: Geochimica et Cosmochimica Acta, v. 34, no. 1, p. 105–120. [also available at https://doi.org/10.1016/0016-7037(70)90154-7.]

Peucker-Ehrenbrink, B., and Fiske, G.J., 2019, A continental perspective of the seawater $^{87}Sr/^{86}Sr$ record—A review: Chemical Geology, v. 510, p. 140–165. [also available at https://doi.org/10.1016/j.chemgeo.2019.01.017.]

Rigsby, C.A., 1998, Paleogeography of the western Transverse Range Province, California—New evidence from the late Oligocene and early Miocene Vaqueros Formation, chap. T *of* Keller, M.A., ed., Evolution of sedimentary basins/onshore oil and gas investigations—Santa Maria Province: U.S. Geological Survey Bulletin 1995–T, U, V, p. T1–T18, accessed October 7, 2021, at https://doi.org/10.3133/b1995TUV.

Rosenbauer, R.J., Foxgrover, A.C., Hein, J.R., and Swarzenski, P.W., 2013, A Sr-Nd isotopic study of sand-sized sediment provenance and transport for the San Francisco Bay coastal system: Marine Geology, v. 345, p. 143–153, accessed March 18, 2022, at https://doi.org/10.1016/j.margeo.2013.01.002.

Stanley, R.G., Valin, Z.C., and Pawlewicz, M.J., 1992, Rock-Eval pyrolysis and vitrinite reflectance results from outcrop samples of the Rincon Shale (lower Miocene) collected at the Tajiguas Landfill, Santa Barbara County, California: U.S. Geological Survey Open-File Report 92–571, 27 p., accessed October 2, 2021, at https://pubs.usgs.gov/of/1992/0571/report.pdf.

Taylor, J.D., Kennedy, W.J., and Hall, A., 1969, The shell structure and mineralogy of the Bivalvia: Bulletin of the British Museum of Natural History Zoology Supplement 3, 125 p., 29 plates.

Ullmann, C.V., and Korte, C., 2015, Diagenetic alteration in low-Mg calcite from macrofossils—A review: Geological Quarterly, v. 59, no. 1, p. 3–20, accessed March 15, 2022, at https://doi.org/10.7306/gq.1217.

Veizer, J., 1983, Trace elements and isotopes in sedimentary carbonates, chap. 8 *of* Reeder, R.J., ed., Carbonates—Mineralogy and chemistry, Reviews in Mineralogy 11: Berlin, Boston, DeGruyter, p. 265–300. [also available at https://doi.org/10.1515/9781501508134-012.]

Veizer, J., Buhl, D., Diener, A., Ebneth, S.O.G., Podlaha, O.G., Bruckschen, P., Jasper, T., Korte, T., Schaaf, M., Ala, D., and Azmy, K., 1997, Strontium isotope stratigraphy—Potential resolution and event correlation: Palaeogeography, Palaeoclimatology, Palaeoecology, v. 132, no. 1–4, p. 65–77, accessed October 4, 2021, at https://doi.org/10.1016/S0031-0182(97)00054-0.

Weaver, D.W., and Doerner, D.P., 1969, Lower Tertiary stratigraphy of San Miguel and Santa Rosa Islands, *in* Weaver, D.W., Doerner, D.P., and Nolf, B., eds., Geology of the Northern Channel Islands—American Association of Petroleum Geologists and Society of Economic Paleontologists and Mineralogists Pacific Sections. Special Publication, p. 30–47.

Weaver, D.W., Doerner, D.P., and Nolf, B., 1969, Geology of the Northern Channel Islands: Los Angeles, California, American Association of Petroleum Geologists and Society of Economic Paleontologists and Mineralogists Pacific Sections, Special Publication, 200 p., 3 geologic maps, scale 1:24,000.

Woolley, J.J., 1998, Sedimentology of the Oligocene Sespe and Vaqueros Formations, Santa Rosa Island, California, *in* Weigand, P.W., ed., Contributions to the geology of the Northern Channel Islands, southern California: Bakersfield, California, American Association of Petroleum Geologists Pacific Section Annual Meeting MP-45, p. 77–89. [also available at https://doi.org/10.32375/1998-MP45.5.]

Publishing support provided by the Science Publishing Network,
Reston and Denver Publishing Service Centers

For more information concerning the research in this report, contact the

Center Director, USGS Geosciences and Environmental Change Science Center
Box 25046, Mail Stop 980
Denver, CO 80225
(303) 236-5344

Or visit the Geosciences and Environmental Change Science Center website at https://www.usgs.gov/centers/gecsc

ISSN 2328-0328 (online)
https://doi.org/10.3133/sir20235026